Research Square

Preprints are preliminary reports that have not undergone peer review.
They should not be considered conclusive, used to inform clinical practice,
or referenced by the media as validated information.

Tailoring Crystal Structure, Optical Band and Wettability of Green-Synthesized BiOI Nanoparticles via pH-Controlled Hydrothermal Method

Avanish Mishra
Madan Mohan Malaviya University of Technology
Satya Pal Singh
singh.satyapal.pmsd@gmail.com
Madan Mohan Malaviya University of Technology

Research Article

Keywords: BiOI nanoparticles, Green hydrothermal synthesis, pH engineering, Crystal phase evolution, Bandgap tuning, Surface wettability, Zeta potential, Structure–property relationship

Posted Date: November 3rd, 2026

DOI: https://doi.org/10.21203/rs.3.rs-11304048/v1

License: This work is licensed under a Creative Commons Attribution 4.0 International License.
Read Full License

Additional Declarations: No competing interests reported.

Tailoring Crystal Structure, Optical Band and Wettability of Green-Synthesized BiOI Nanoparticles via pH-Controlled Hydrothermal Method

Avanish Mishra, Satya Pal Singh*
Condensed Matter Physics & Nanoscience Research Laboratory
Department of Physics and Material Science
Madan Mohan Malaviya University of Technology, Gorakhpur, India
Corresponding author. E –mail address*: singh.satyapal.pmsd@gmail.com, singh.satyapal@hotmail.com

Abstract:

In this study, BiOI nanoparticles were synthesized through a green hydrothermal route using Murraya koenigii (curry leaf) extract, with the reaction pH systematically varied from 5 to 13. to investigate its influence on the structural, morphological, optical, surface-charge, and wettability characteristics. X-ray diffraction analysis showed that BiOI retained a tetragonal structure at pH 5–10, whereas a structural transformation toward an orthorhombic phase was observed under strongly alkaline conditions at pH 13. The crystallite size varies from 18.67±4.86 to 30.37±11.34 nm, accompanied by changes in crystallinity, lattice strain, and defect density. Scanning electron microscopy revealed a pronounced morphological evolution from cauliflower-like aggregates to hierarchical flower-like structures and subsequently to larger plate/rod-like features with increasing pH, indicating the influence of solution chemistry on crystal growth and aggregation. FTIR analysis identified characteristic vibrational features of Bi–O–I nanoparticle framework and surface functional groups. UV–Vis analysis revealed pH-dependent optical band gaps, with indirect values of 1.607 ± 0.005–2.202 ± 0.011 eV and direct values of 2.170 ± 0.012–2.523 ± 0.009 eV. The zeta potential became increasingly negative from −30.93 ± 1.61 to −40.83 ± 0.34 mV, while the water contact angle decreased from 53.57 ± 2.23° to 23.03 ± 2.29°, indicating systematic changes in surface charge and wettability. Thus, reaction pH provides an effective route to tune the structural, morphological, optical, and interfacial properties of BiOI-based materials, offering potential for photocatalytic, photo-electrochemical, optoelectronic, self-cleaning, and atmospheric water-harvesting applications.

Keywords- BiOI nanoparticles, Green hydrothermal synthesis, pH engineering, Crystal phase evolution, Bandgap tuning, Surface wettability, Zeta potential, Structure–property relationship.

1. Introduction

Bismuth-based semiconductor materials have emerged as promising visible-light-responsive photocatalysts owing to their tunable band gaps, excellent chemical stability, and environmentally benign nature. Among them, the bismuth oxyhalide (BiOX; X = Cl, Br, I) family has attracted considerable attention because of its layered crystal structure, remarkable optical properties, and broad applications in environmental remediation, photoelectrochemical conversion, solar-energy harvesting, gas sensing, antibacterial coatings, optoelectronic devices, and atmospheric water harvesting. Consequently, extensive efforts have been devoted to tailoring the structural and surface characteristics of BiOX nanomaterials through rational synthesis strategies [1–3]. Among the BiOX family, bismuth oxyiodide (BiOI) has emerged as one of the most attractive members because of its relatively narrow band gap (~1.7–2.0 eV) and efficient visible-light absorption. BiOI crystallizes in a tetragonal matlockite structure (space group P4/nmm*)* consisting of alternating positively charged $[Bi_2O_2]^{2+}$ slabs and iodide layers linked by weak van der Waals interactions [4–6]. This layered architecture generates an intrinsic internal electric field that promotes efficient separation of photo-generated electron–hole pairs, suppresses charge recombination, and enhances visible-light activity, making BiOI highly suitable for sustainable environmental and energy-related applications [1,4,5–9]. The physicochemical properties of BiOI are strongly influenced by its crystal structure, crystallinity, morphology, particle size, exposed crystal facets, and defect concentration. Various synthesis methods have therefore been developed to tailor these characteristics; however, solution pH remains one of the most influential parameters governing Bi^{3+} hydrolysis, nucleation, crystal growth, phase evolution, and defect formation [10–12]. The synthesis pH plays a crucial role in governing the nucleation, crystal growth, and microstructural evolution of BiOI nanoparticles, thereby influencing their crystallinity, morphology, optical response, and surface properties [11]. Despite numerous studies on BiOI, a comprehensive understanding of the relationship between pH-controlled crystal growth and the resulting structure–property correlations remains limited [11]. Furthermore, plant-mediated green synthesis has attracted considerable attention as an environmentally sustainable approach, in which naturally occurring phytochemicals act as reducing, capping, and stabilizing agents, enabling the preparation of nanomaterials without the use of toxic chemicals or synthetic surfactants [12].

The physicochemical properties and functional performance of BiOI are strongly governed by its crystal morphology, crystallographic orientation, particle size, defect density, and surface chemistry. Accordingly, considerable efforts have focused on controlling precursor concentration, reaction temperature, reaction time, solvent composition, mineralizers, surfactants, and particularly solution pH, which regulates Bi^{3+} hydrolysis, supersaturation, nucleation kinetics, crystal growth, and phase stability [5,10,13]. Even slight variations in pH can significantly influence crystallinity, exposed crystal facets, morphology, defect concentration, and consequently the optical and surface properties of BiOI nanoparticles [5,10–11]. Previous studies have shown that acidic conditions generally favour the formation of compact flower-like or micro-spherical BiOI architectures, whereas alkaline media promote anisotropic crystal growth, crystallite coarsening, and morphological evolution toward rod-like and plate-like assemblies through pH-dependent crystal growth kinetics [10–16]. Such pH-controlled structural evolution significantly influences the crystallinity, crystallite size, defect distribution, optical response, and surface properties of BiOI, thereby affecting its visible-light absorption and interfacial characteristics. However, a comprehensive understanding of the relationship between pH-controlled crystal growth, morphology, crystallinity, surface chemistry, and wettability remains limited. Recent investigations have further demonstrated that lattice defects, structural disorder, and surface functional groups play important roles in regulating the physicochemical properties of BiOI by modifying its electronic structure and visible-light absorption characteristics [11,15–17]. Moreover, morphology-dependent variations in surface roughness, active-site density, adsorption behaviour, and surface energy significantly influence the interaction of BiOI with aqueous environments, highlighting the importance of simultaneously correlating crystal structure and surface characteristics. Green synthesis has recently emerged as a sustainable alternative to conventional hydrothermal and solvothermal methods. Plant-derived phytochemicals, including polyphenols, flavonoids, alkaloids, terpenoids, carbohydrates, and proteins, act as natural reducing, complexing, and stabilizing agents during nanoparticle formation

[12,17]. Although plant-mediated synthesis has been widely explored for photocatalytic applications, systematic investigations correlating pH-controlled structural evolution, defect chemistry, colloidal stability, surface wettability, and optical properties remain scarce.

Most published studies explain the structural evolution of BiOI nanostructures using only a limited number of characterization techniques, primarily X-ray diffraction, electron microscopy, and UV–visible spectroscopy [10–17]. However, comprehensive investigations integrating XRD, FTIR, SEM–EDX, UV–Vis absorption spectroscopy, Tauc analysis, zeta potential, and contact-angle measurements under identical synthesis conditions remain scarce. Since crystal structure, chemical bonding, morphology, colloidal stability, optical absorption, and surface wettability are intrinsically interconnected, establishing a direct correlation between pH-induced crystal evolution and these physicochemical properties is essential for the rational design of multifunctional BiOI nanomaterials for environmental remediation, photocatalysis, antibacterial coatings, self-cleaning surfaces, and atmospheric water-harvesting applications. Despite considerable advances in hydrothermal, solvothermal, precipitation, and green synthesis routes, several fundamental challenges remain unresolved. Most previous studies have primarily focused on photocatalytic degradation while comparatively little attention has been devoted to understanding how solution pH simultaneously governs crystal phase evolution, morphology, crystallinity, optical behaviour, colloidal stability, and wettability. Consequently, the lack of a comprehensive structure–property relationship limits the development of BiOI-based multifunctional materials for advanced environmental and energy-related applications [4,5,12,18,19]. Moreover, although green plant-mediated synthesis has gained increasing attention, systematic pH-controlled synthesis of BiOI remains insufficiently explored. Plant-derived phytochemicals act as natural reducing and stabilizing agents, yet their influence on phase stability, defect formation, crystal evolution, and surface functionality has not been comprehensively established [5,18–19]. Another major limitation is the absence of integrated characterization capable of correlating structural evolution with surface physicochemical properties. Parameters such as zeta potential, contact angle, FTIR, EDX, and optical band structure are equally important because they govern particle dispersion, interfacial interactions, aqueous stability, and multifunctional surface performance [17–21]. Furthermore, a comprehensive understanding of how synthesis pH simultaneously governs the crystal growth, crystallinity, morphology, optical band gap, colloidal stability, surface chemistry, and wettability of green-synthesized BiOI nanoparticles remains limited, despite the strong interrelationship among these physicochemical properties and their importance for functional applications [18–22].

In the present work, BiOI nanoparticles were synthesized through an environmentally benign hydrothermal approach using curry leaf (Murraya koenigii) extract as a plant-derived component under four different pH conditions (5, 8, 10, and 13). The influence of synthesis pH on the crystal structure, crystallinity, morphology, elemental composition, chemical bonding, optical absorption, surface charge, colloidal stability, and wettability was systematically investigated using X-ray diffraction (XRD), scanning electron microscopy coupled with energy-dispersive X-ray spectroscopy (SEM–EDX), Fourier-transform infrared spectroscopy (FTIR), UV–Visible spectroscopy, Tauc analysis, zeta potential measurements, and contact-angle analysis. Rather than attributing novelty solely to the pH-dependent evolution of BiOI, which has been explored in previous studies, the present work focuses on the integrated experimental assessment of structural, morphological, optical, and interfacial changes produced by varying the synthesis pH within a green hydrothermal system. The results provide a comparative view of the synthesis–structure–property relationships of BiOI, including the observed structural transformation under strongly alkaline conditions and the accompanying changes in morphology, surface charge, optical response, and wettability. These observations may be useful for understanding and controlling the physicochemical characteristics of BiOI through synthesis conditions. The present study therefore provides a systematic experimental framework for examining the influence of reaction pH on multiple properties of green-synthesized BiOI nanoparticles. The combined characterization results help clarify how changes in solution chemistry are associated with variations in crystal structure, morphology, surface characteristics, and optical behaviour. Such information may be relevant to the further development of BiOI-based materials for applications such as photocatalysis, photo-electrochemical systems, optoelectronics, self-cleaning surfaces, and atmospheric water harvesting; however, these potential applications were not directly evaluated in the

present study and require dedicated experimental investigation. The main contribution of this work is thus the comparative correlation of pH-dependent structural and morphological evolution with optical, surface-charge, and wettability characteristics of BiOI synthesized using a plant-assisted hydrothermal route, providing a basis for further studies on the application-specific performance of these materials.

2. Materials and Method

Bismuth nitrate pentahydrate ($Bi(NO_3)_3 \cdot 5H_2O$; (13.78 g) was dissolved in 100 mL of distilled water and magnetically stirred at 600 rpm for 30 min to ensure complete dissolution. Separately, sodium iodide (NaI; 4.71 g) was dissolved in 100 mL of distilled water and stirred at 600 rpm for 30 min. Fresh curry leaves (50 g) were dried at 50 °C until completely dry. The dried leaves were then ground into a fine powder using a mortar and pestle. The resulting powder was dispersed in 50 mL of distilled water and stirred continuously for 2 h at room temperature to obtain the curry leaf extract. The mixture was subsequently filtered through filter paper to remove the insoluble plant residues, and the obtained filtrate was collected in a clean beaker for further use in the synthesis process. The preparation of curry leaf extract is schematically illustrated in Figure 1.(a). Subsequently, both solutions [($Bi(NO_3)_3 \cdot 5H_2O$ and NaI] were combined under constant stirring, and 50 mL of freshly prepared curry leaf extract was added to the mixture. The reaction proceeded for an additional 30 min at 600 rpm to facilitate uniform blending of the precursors. The pH of the resulting solution was adjusted to 5, 8, 10, and 13 by careful dropwise addition of sodium hydroxide (NaOH), allowing for the controlled investigation of pH-dependent synthesis. The final reaction mixture was transferred into a Teflon-lined stainless-steel autoclave and subjected to hydrothermal treatment at 180 °C for 18 h. Upon cooling to room temperature, the resulting precipitate was collected via centrifugation at 3200 rpm for 20 min. The isolated material was washed thoroughly with distilled water to remove any residual ions and then oven-dried at 60 °C for 48 h to obtain the final BiOI nanomaterials. Figure.1 (b). shows the preparation of BiOI nanomaterials via the hydrothermal method. For zeta potential measurements, 5 mg of BiOI/Bi_5O_7I nanoparticles was dispersed in 20 mL of distilled water, corresponding to a concentration of 0.25 mg/mL, and the resulting suspension was thoroughly mixed before measurement. For water contact angle measurements, 10 mg of BiOI nanoparticles was dispersed in 20 mL of distilled water and ultrasonicated for 30 min at 50 °C to obtain a homogeneous suspension. A clean glass slide was placed horizontally in a suitable tray, and the prepared BiOI/Bi_5O_7I suspension was poured uniformly over the glass substrate. The coated substrate was subsequently dried at 60 °C for 12 h to obtain a BiOI-coated surface. The water contact angle was then measured on the dried BiOI-coated substrate to evaluate its surface wettability.

3. Results and Analysis

3.1. Structural Analysis

3.3.1 X-ray diffraction (XRD) Analysis

The analysis of the nanostructural properties of the prepared sample within the scanning angle range of 20° to 60° was performed using X-ray powder diffraction (model: D8 Advance Eco, BBAU) using CuKα (1.5406 Å) radiation. The XRD patterns of the BiOI nanoparticles synthesized by maintaining reaction pH values of 5, 8, 10, and 13 are shown in Fig. 2 (a–d). For the samples synthesized at pH 5,8 and 10 the distinct diffraction peaks observed at various 2θ angles correspond to the characteristic reflection planes of pure BiOI (JCPDS No. 10-0445), confirming a highly crystalline tetragonal structure. Conversely, as the synthesis medium becomes highly alkaline i.e. pH 13, the pure BiOI phase completely collapses, resulting in the absolute formation of a highly crystalline orthorhombic Bi_5O_7I phase (JCPDS No. 40-0548). A comparison of the measured and standard values of the d-spacing for the (hkl) planes further verified that BiOI exhibited a tetragonal polycrystalline structure. The absence of any major impurity peaks in the pH 5–10 samples indicates the successful formation of phase-pure BiOI nanostructures, suggesting that controlled pH conditions effectively regulate the hydrolysis-condensation kinetics during crystal growth.

For the tetragonal planes, the lattice parameters were evaluated using the following relation [23]:

$$\frac{1}{d_{hkl}^2} = \left[\frac{h^2+k^2}{a^2}\right] + \left(\frac{l^2}{c^2}\right) \quad (1)$$

For the orthorhombic planes, the lattice parameters were evaluated using the following relation [24]:

$$\frac{1}{d_{hkl}^2} = \frac{h^2}{a^2} + \frac{k^2}{b^2} + \frac{l^2}{c^2} \quad (2)$$

Table 2 represents the lattice parameter values for BiOI. The crystallite size (D) was determined using the Debye-Scherrer formula (Eq. (2)) [25]:

$$D = \frac{K\lambda}{\beta \cos\theta} \quad (2)$$

In the above equation, the FWHM of the diffraction peaks is denoted as full width half maximum and is expressed in radians, symbolized as β. In this experiment, λ is the X-ray wavelength, and θ (Bragg angle) is the angle at which diffraction occurs according to Bragg's Law.

Equation (3) was employed to ascertain the strain (ϵ) [25]:

$$\epsilon = \frac{\beta}{4\mathrm{Tan}\theta} \quad (3)$$

The parameter δ often known as dislocation density is the total length of dislocation lines in a unit volume of the crystal, calculated employing equation. (4) [25]:

$$\delta = \frac{1}{D^2} \quad (4)$$

The effects of reaction pH on the phase purity, crystal structure development, and structural properties of BiOI/Bi_5O_7I nanoparticles obtained through a green chemistry method were analyzed using X-ray diffraction (XRD). It should be noted that the diffraction spectra reveal the fact that pH of the reaction solution plays a significant role in controlling crystal nucleation, ordering, and crystallite growth. The systematic changes in the diffraction spectrum with increasing pH indicate the structural tuning of BiOI through the influence of pH on the crystallization process. The X-ray diffraction patterns (Figure.2) reveal a clear pH-dependent evolution of the crystalline structure of the synthesized BiOI/Bi_5O_7I. The diffraction peaks observed for the samples prepared at pH 5, 8, and 10 are consistently indexed to the characteristic reflections of tetragonal BiOI, confirming the formation of a well-defined tetragonal phase within this pH range. The corresponding 2θ values, interplanar spacing (d), and crystallographic (hkl) planes are presented in Table 1. The observed variations in peak position with synthesis pH indicate changes in the crystallographic environment and crystallite characteristics associated with the pH-dependent nucleation and growth of BiOI. In particular, the differences in peak broadening suggest variations in crystallite size and lattice disorder among the samples. At pH 13, however, the diffraction pattern undergoes a pronounced structural change, with the appearance of additional reflections that are not consistent with the tetragonal BiOI phase [24]. These reflections indicate the development of an orthorhombic Bi_5O_7I phase under the strongly alkaline synthesis condition. This structural evolution suggests that the tetragonal BiOI phase is preferentially stabilized between pH 5 and 10, whereas the highly alkaline environment at pH 13 alters the nucleation and growth pathway and promotes a tetragonal-to-orthorhombic phase transformation. Therefore, the XRD results demonstrate that synthesis pH plays a decisive role in controlling the phase stability and crystallographic evolution of BiOI.

The results of the calculation of structural parameters, such as crystallite size, lattice strain, dislocation density, crystallinity %, and lattice parameters, are listed in Table 2. As shown in Fig. 2 (a,b,c) the diffraction spectrum of the sample obtained by maintaining pH 5, pH 8 and pH 10 demonstrates well-defined peaks corresponding to the reflection of the tetragonal form of BiOI, which includes (101), (102), (110), (004), (200), (212); (101),(102),(110), (103), (104), (200), (211/055), (211) and (001), (101), (102), (110), (112), (200), (212) crystallographic planes respectively, indicating the successful formation of pure-phase BiOI (JCPDS no. 10-0445 and 73-2062) [26,27]. The diffraction peaks of the samples synthesized at pH 5, pH 8, and pH 10 indicating the formation of nanocrystals with crystallite size of 25.30±7.82, 18.67±4.86, and 20.37±4.86 nm respectively. The relatively sharp and intense diffraction peaks indicate enhanced crystallinity and larger crystallite sizes, suggesting that crystal growth predominated over nucleation during the hydrothermal synthesis process under the optimized reaction conditions [28]. Consequently, the sample synthesized at pH 5 exhibited a crystallinity of 97.75% and a dislocation density of 2.09×10^{15} m^{-2}, indicating a relatively lower density of lattice defects compared with the samples synthesized at pH 8 and 10. The relatively low value of the lattice strain 5.27×10^{-3} shows that crystal growth does not occur completely, which is confirmed by the morphology of the cauliflower-like aggregates in the SEM images. Compared with the BiOI nanoparticles synthesized by maintaining the reaction pH at 5, the diffraction spectrum of the sample obtained by maintaining pH 8 also demonstrates well-defined peaks corresponding to the reflection of the tetragonal form of BiOI. As the synthesis pH increased from 5 to 8, a slight decrease in crystallite size to 18.67 ± 4.86 nm and crystallinity to 92.42% was observed, accompanied by an increase in lattice strain to 6.14×10^{-3} and dislocation density to 3.46×10^{15} m^{-2} [29]. This behavior suggests that maintaining the reaction pH at 8 provides favorable conditions for the nucleation and crystal growth of BiOI, resulting in relatively well-ordered crystalline domains while limiting excessive particle aggregation. The combination of relatively high crystallinity (92.42%) and a crystallite size of 18.67 ± 4.86 nm indicates the formation of well-crystallized nanoscale domains with comparatively low structural disorder. These structural characteristics may contribute to the formation of the hierarchical architectures observed in the SEM images. The BiOI nanoparticles synthesized at pH 8 therefore exhibited favorable structural ordering and crystallinity, as evidenced by the XRD analysis [30]. Notably, the characteristic (001) reflection for pH 8 at $2\theta = 12.41°$ exhibits comparatively broad peak width, with an FWHM of 1.25°. The pronounced broadening of this reflection may be associated with the small coherent crystallite dimensions and the anisotropic growth characteristics of the layered BiOI structure. Considering the layered crystal structure of BiOI and the corresponding SEM observations, this behavior is consistent with the formation of nanoscale plate-like or sheet-like structural features. However, the XRD peak broadening alone is not considered definitive evidence of a specific morphology. The sample synthesized by maintaining the reaction pH 10, accompanied by a sudden decrease of crystallinity to 86.92%, with the crystallite size slightly increasing to 20.37±4.86 nm. However, the structural rearrangement in the highly alkaline environment induced considerable lattice stress, yielding a microstrain of 7.12×10^{-3} and a dislocation density of 2.96×10^{15} m^{-2}. These observations suggest that crystal growth becomes dominant under mildly alkaline conditions, where the coarsening of larger crystallites at the expense of smaller ones is consistent with an Ostwald ripening growth mechanism [31]. This observation is consistent with the SEM results, which show a transition from flower-like structures toward more compact plate-like and thicker sheet-like morphologies at higher pH. These results suggest that pH 10 provides favorable conditions for the development of the observed BiOI morphology [32]. Under extremely alkaline conditions at pH 13 (Fig. 2d), a complete phase transformation occurred, marking the absolute collapse of the pure BiOI framework and the emergence of a highly crystalline orthorhombic Bi_5O_7I phase. The diffraction spectra displayed distinct new peaks corresponding to the (200), (312), (004), (204), (020), (023), (315), (622), and (516) reflection planes [JCPDS No. 40-0448 and 40-0445] [32-33]. While the overall crystallinity increased to 95.37 %, the crystallite size increased significantly to 30.37±11.34 nm. This structural rearrangement yielded the lowest dislocation density 1.80×10^{15} m^{-2} among all samples alongside a notable microstrain of 4.39×10^{-3}. The presence of this lattice strain, even within larger grown crystals, is attributed to the aggressive alkaline environment facilitating continuous dissolution and recrystallization during hydrothermal synthesis [28]. These structural modifications perfectly corroborate the morphological shifts observed via SEM, illustrating a transition from hierarchical flower-like architectures to enlarged block-like and sheet-like structures. The lattice parameter ‘a’ of tetragonal BiOI remained nearly constant at 3.98 Å for pH 5 and pH 8, but decreased to 3.87 Å at pH 10, indicating a slight change in the lattice structure at higher pH. In contrast, the lattice

parameter of tetragonal BiOI, ‘c’, exhibited a non-monotonic variation with increasing pH. The c value increased from 9.23 Å at pH 5 to 9.45 Å at pH 8, followed by a pronounced decrease to 8.75 Å at pH 10. This variation suggests that changes in the synthesis pH influence the lattice arrangement and local structural environment of BiOI, resulting in pH-dependent distortion or rearrangement of the crystal lattice [34]. At pH 13, the tetragonal BiOI phase undergoes a pronounced structural transformation toward an orthorhombic Bi_5O_7I phase. The resulting orthorhombic structure is characterized by lattice parameters of a = 16.09 Å, b = 5.34 Å, and c = 11.46 Å, confirming the significant pH-induced change in the crystal structure of BiOI under strongly alkaline conditions. The XRD analysis indicates that the pH plays a critical role in controlling the phase evolution, lattice distortion, crystallinity, and defect chemistry of BiOI nanostructures, thus governing their functional surface and optical properties.

3.2. Surface Chemistry and Functional Groups

3.2.1. Fourier Transform Infrared (FTIR) Spectroscopy

FTIR spectra were recorded using a Spectrum Two FTIR spectrometer (PerkinElmer Inc., Waltham, MA, USA) at the Malaviya National Institute of Technology (MNIT), Jaipur, India. The FTIR spectra of the BiOI/Bi_5O_7I nanoparticles synthesized by maintaining reaction pH values of 5, 8, 10, and 13 are shown in Fig. 3(a–d). Specific absorption peaks were observed in the FTIR spectra owing to OH groups, adsorbed water molecules, precursor species, and Bi–O/Bi–I lattice vibrations. Although there are commonalities in all the FTIR spectra, the variation in the positions and intensities of the peaks shows that the reaction pH level influences the bonding, growth mechanisms, and surface chemistry of the BiOI/ Bi_5O_7I nanoparticles. This is consistent with the results obtained from XRD, SEM, UV–Vis, zeta potential, and contact angle analyses. The specific FTIR absorption peaks of the BiOI/ Bi_5O_7I nanoparticles synthesized at various reaction pH levels, together with their vibrational assignments, are listed in Table 3. The observed FTIR absorption peaks confirm the formation of the BiOI/ Bi_5O_7I framework and indicate that the pH level leads to changes in local bonding, surface hydroxylation, and lattice vibrations, which can be correlated with structural and morphological changes observed from the XRD and SEM analyses. The FTIR spectrum of the BiOI nanoparticles synthesized by maintaining the reaction pH at 5 (Fig. 3a) displays a broad absorption band centered at 3423.49 cm^{-1}, which is may be attributed to due to the O–H stretching vibration of surface hydroxyl groups and residual phytochemicals from the curry leaf extract [35-37]. The peak at 1628.47 cm^{-1} is attributed to the H–O–H bending vibration of adsorbed water molecules [35] that indicates the hydrophilicity of the nanoparticle surface. The peak at 1383.95 cm^{-1} belongs to the asymmetric stretching vibration of NO_3^- ion species from the bismuth nitrate precursor, implying the trace residual of nitrate species after crystallization [35]. The absorption peak at 1012.09 cm^{-1} corresponds to the Bi–O stretching vibrations in the $[Bi_2O_2]$ layer of the BiOI structure, whereas the peak at 838.80 cm^{-1} corresponds to the Bi–O–I lattice vibrations of tetragonal BiOI [32-33]. The low-frequency peaks at 666.54 and 536.72 cm^{-1} correspond to Bi–O and Bi–I lattice vibrations, respectively, confirming the successful formation of the BiOI framework [35]. The relatively broad Bi–O and Bi–I peaks are in accordance with the lower crystallinity and cauliflower-like aggregated morphology observed in the XRD and SEM analyses. In the case of BiOI nanoparticles synthesized by maintaining the reaction pH at 8 (Fig. 3b), the O-H stretching peaks shifted to 3247.89 cm^{-1}, demonstrating that there were modifications in the hydrogen bonds and surface hydroxyls formed during the crystallization process. The absorption peak for H-O-H bending shifted to 1633.34 cm^{-1}, while the nitrate band remained almost constant at 1382.88 cm^{-1}, demonstrating that the conversion of the precursor was performed efficiently [29]. The Bi–O stretching vibration shifted to 1058.01 cm^{-1}, suggesting a strengthened Bi–O coordination environment under alkaline conditions. Furthermore, the intensified Bi–O–I vibration at 846.86 cm^{-1} and the sharper Bi–I lattice vibration at 548.89 cm^{-1}, compared with BiOI nanoparticles synthesized by maintaining the reaction pH at 5, indicate improved structural ordering and enhanced crystallinity [36].

These changes are consistent with the XRD and SEM results, which indicate relatively high crystallinity and the formation of flower-like hierarchical nanostructures under moderately alkaline conditions. The FTIR spectrum of the

BiOI nanoparticles synthesized by maintaining the reaction pH 10 and Bi_5O_7I nanoparticles synthesized by maintaining pH 13 (Fig. 3 c & d) exhibits a broad absorption band centered at 3432.43 cm^{-1} and 3458.54 cm^{-1} respectively, which may also arises due to the presence of abundant surface hydroxyl groups originating from the nanoparticle surface and residual phytochemicals of the curry leaf extract [37].The absorption peaks at 1631.76 cm^{-1} and 1382.83 cm^{-1} correspond to adsorbed water and nitrate, respectively, which proves that the conversion process was performed efficiently [32]. The Bi-O stretching peak is shifted to 1015.89 cm^{-1}, while there are two characteristic lattice vibrations at 897.39 and 844.37 cm^{-1}, respectively. Moreover, there are two low-frequency vibration peaks at 536.47 and 455.52 cm^{-1}, which are assigned to Bi-I and lattice Bi-O vibrations, respectively [36,38]. The FTIR spectrum of the BiOI nanoparticles synthesized by maintaining the reaction pH 13 (Fig. 3d) exhibits the vibration of H-O-H bending is observed at 1634.99 cm^{-1}, whereas the vibration of the nitrate band is observed at 1384.26 cm^{-1} [35]. The Bi-O stretching vibration shifts to 1060.68 cm^{-1}, along with an additional vibration at 996.60 cm^{-1}, which shows a change in the Bi-O bonding environment. The vibration of the lattice at 847.43 cm^{-1} indicates the retention of the Bi-O-I framework. Most importantly, the vibrations at low frequencies of 611.86, 570.41, and 504.36 cm^{-1} show the strengthening of Bi-O lattice vibrations in a highly alkaline medium [. This observation is consistent with the XRD results, which reveal enhanced crystallinity and crystal growth under strongly alkaline conditions, indicating that the increased alkalinity significantly influences the structural and morphological evolution of BiOI nanoparticles.

3.3. Morphological and Elemental Analysis

3.3.1. Scanning Electron Microscopy (SEM) Analysis

The surface morphologies of the green-synthesized BiOI nanoparticles synthesized at different pH values were studied using scanning electron microscopy (SEM) (Model- JSM 6490LV, BBAU Lucknow). The SEM micrographs of the BiOI/ Bi_5O_7I nanoparticles synthesized by maintaining the reaction pH at 5, 8, 10, and 13 are presented in Fig. 4(a–h). The SEM studies clearly show a distinctive pH-dependent morphological development process in the green synthesis of BiOI nanoparticles. This shows that the pH level of the reaction is an important parameter in controlling the nucleation rate, crystal growth, self-assembly, and phase stability of BiOI/ Bi_5O_7I nanoparticles. The changes in morphology are consistent with the XRD results, which show that the structure and size of the crystallites depend on the pH level of the synthesis. In particular, Fig.4 (a-b) shows that the BiOI nanoparticles synthesized by maintaining pH 5 have a highly agglomerated moss rose flower-like microsphere made up of many small nanoparticles [26]. The rough surface features and irregular particle boundaries indicate a fast nucleation process under acidic conditions. The fast hydrolysis of Bi^{3+} ions causes a high nucleation rate, leading to many nuclei within a short time [39]. The incomplete crystal growth process leads to the formation of many primary nanoparticles, which tend to aggregate to minimize the surface energy and form a compact cauliflower-like structure [26,36]. The BiOI nanoparticles synthesized by maintaining the reaction pH 8 (Fig. 4c–d) exhibit well-developed cauli-flower-like hierarchical microspheres composed of interconnected ultrathin nanosheets, indicating controlled anisotropic crystal growth and hierarchical self-assembly. Thus ultrathin nanosheets appear, and then self-assembly of them in flower-like structures occurs. It is worth noting that the crystallite size at pH 8 (18.67 ± 4.86 nm) is comparatively smaller than those obtained at the other investigated pH conditions, whereas the SEM images show relatively larger hierarchical structures. This difference can be attributed to the formation of secondary assemblies composed of multiple nanoscale crystallites, as SEM primarily reflects the overall particle morphology rather than individual coherent crystallite domains determined by XRD.

The BiOI nanoparticles synthesized at pH 8 exhibited relatively higher crystallinity and good structural characteristics, as indicated by the XRD analysis. These features suggest favorable conditions for the formation of BiOI with a well-defined crystalline structure. The BiOI nanoparticles synthesized by maintaining the reaction pH at 10 (Fig. 4e–f) exhibit interconnected rod-like crystallites that gradually self-assemble into larger plate-like architectures, indicating

the predominance of crystal growth and oriented attachment under mildly alkaline synthesis conditions. This morphological evolution indicates that the alkaline medium promoted the oriented attachment and coalescence of neighboring crystallites, resulting in a denser and more ordered microstructure than that observed for the BiOI nanoparticle synthesized by maintaining pH 8. These observations were consistent with the XRD results, which showed a crystallite size of 20.37±4.86 nm and relatively lower crystallinity compared with the other synthesized samples. The SEM micrographs of the BiOI nanoparticles synthesized by maintaining the reaction pH at 13 (Fig. 4g–h) reveal a pronounced morphological evolution, in which the well-defined hierarchical flower-like and rod like architecture transformed into densely agglomerated plate or sheet-like structures with a few elongated rod-like crystallites, indicating significant crystal coarsening under highly alkaline synthesis conditions. The larger plates appear to be decorated with numerous fine crystallites, producing compact aggregates with considerably lower porosity than those observed at lower pH values. The morphological evolution observed in the SEM micrographs is in good agreement with the XRD analysis. The increase in crystallite size from 20.37±4.86 nm at pH 10 to 30.37±11.34 nm at pH 13, together with the reduction in dislocation density to 1.80×10^{15} m^{-2} , indicates that crystal coarsening became dominant under highly alkaline synthesis conditions [34]. This crystallographic evolution is reflected in the SEM images by the disappearance of the well-defined hierarchical flower-like architecture and the formation of densely packed plate-like and sheet-like structures with a few elongated rod-like crystallites. The morphological features observed by SEM are in good agreement with the structural characteristics identified by XRD analysis. The relatively broad diffraction peaks observed for the BiOI nanoparticles synthesized at pH 5 correspond to a relatively smaller crystallite size of 25.30 ± 7.82 nm, suggesting the presence of nanoscale crystalline domains with comparatively limited crystallite growth. At pH 8, the crystallite size decreased further to 18.67 ± 4.86 nm, while the diffraction peaks became relatively sharper and more intense, particularly the (102) and (110) reflections, indicating improved crystallographic ordering. These structural characteristics are consistent with the well-defined flower-like hierarchical morphology observed in the SEM images. Upon increasing the reaction pH to 10, the crystallite size increased slightly to 20.37 ± 4.86 nm, accompanied by relatively well-resolved diffraction peaks. This structural evolution is consistent with the compact plate-like and thicker sheet-like features observed in the SEM micrographs, suggesting that the change in pH influences both crystallite development and the resulting hierarchical morphology. At pH 13, the increased crystallite size together with sharper major diffraction peaks reflects crystal coarsening, leading to densely agglomerated plate or sheet-like structures. These results suggest a relationship between the crystallographic changes observed by XRD and the pH-dependent morphological variations observed by SEM [26,36]. Consequently, the SEM and XRD results collectively demonstrate that the synthesis pH plays a decisive role in regulating the crystallite growth, particle aggregation, and morphological evolution of green-synthesized BiOI nanoparticles, thereby enabling controlled tailoring of their microstructure for potential functional applications [6,7].

3.3.2. Energy Dispersive X-ray (EDX) Analysis

To investigate the elemental composition of the BiOI/ nanoparticles greenly synthesized by maintaining pH (5,8,10, and 13), an energy-dispersive X-ray spectroscopy (EDX) analysis was performed, and the respective spectra are shown in Fig. 5(a–d). The results obtained confirmed that the BiOI/ Bi_5O_7I nanoparticles were formed due to the presence of characteristic peaks attributed to Bi, O, and I in all samples, meaning that the hydrothermal synthesis method in combination with curry leaves extract is quite efficient for the production of BiOI/Bi_5O_7I without impurities. Intensive Bi peaks detected at about 2.4, 10.8, and 11.8 keV in addition to I peaks in the range of 3.9–4.3 keV are in line with the characteristic X-ray emission lines of BiOI and corroborate the phase identified based on the results of the XRD analysis [40]. The oxygen peaks appearing at lower energies also confirm the formation of Bi-O bonds characteristic of the BiOI layered crystal structure. The minor carbon (C) signal observed in the EDX spectra may be associated with residual organic components from the curry leaf extract and/or the carbon-based conductive substrate used during SEM analysis.

In addition, the weak Na signal may be associated with residual sodium-containing reagents used during sample preparation, such as NaOH/NaI, whereas the origin of the weak Si signal could not be conclusively identified and may arise from the sample holder, substrate, or other background contributions. These minor signals were not considered characteristic components of the synthesized BiOI nanoparticles. The EDX spectrum of the BiOI sample synthesized at pH 5 (Fig. 5a) exhibited characteristic signals of Bi, O, and I, indicating the presence of the principal constituent elements of BiOI. These elemental observations are consistent with the phase identified by XRD analysis. Relatively intensive Bi peaks along with cauliflower-like agglomerated morphology indicate a fast nucleation process in the acidic environment, leading to dense packing of particles with low crystallinity. The BiOI nanoparticles synthesized by maintaining the reaction pH at 8 (Fig. 5b) exhibit an unchanged elemental composition, while a more homogeneous distribution of Bi, O, and I is observed. The observed elemental distribution is consistent with the cauliflower- like hierarchical morphology seen in the SEM micrographs, suggesting relatively uniform growth under the synthesis conditions. This observation is also consistent with the XRD results, which indicate a crystallite size of 18.67±4.86 nm and comparatively good crystallinity for the sample. Equally intense peaks of Bi and I indicate successful iodide incorporation into the layered structure of BiOI, and the lack of other peaks indicates the high phase purity of the obtained materials. The enhanced homogeneity of the elemental composition is explained by the hydrolysis of Bi^{3+} ions in a moderately alkaline medium, which promotes the anisotropic growth and self-assembly of hierarchical structures [36]. The EDX spectrum of the BiOI nanoparticles synthesized at pH 10 (Fig. 5c) showed prominent signals corresponding to Bi, O, and I, representing the major constituent elements of BiOI. No additional prominent impurity-related signals were observed within the detection limits of the EDX analysis. These elemental observations are consistent with the XRD results, which identified a tetragonal BiOI phase with comparatively higher crystallinity among the synthesized samples. The plate-like morphology observed in the SEM images is accompanied by the observed elemental composition, suggesting that the synthesis conditions at pH 10 may favor the development of this morphology.

The EDX spectrum of the sample synthesized at pH 13 (Fig. 5d) showed signals corresponding to Bi, O, and I, representing the major elements associated with the BiOI-based sample. No prominent additional elemental signals were detected within the limits of the EDX analysis. The observed elemental composition remained broadly consistent despite the changes in crystallite size, crystallinity, and morphology observed under highly alkaline conditions. These structural and morphological variations were identified from the XRD and SEM analyses, respectively. Since EDX provides elemental rather than crystallographic information, the EDX results alone cannot distinguish between different crystal structures or phases [6]. Nevertheless, the SEM images show a pronounced morphological variation from hierarchical flower-like assemblies to more densely agglomerated plate-like and sheet-like structures decorated with fine crystallites. The XRD results also indicate changes in crystallite growth and diffraction peak sharpness at pH 13. These observations suggest that the strongly alkaline synthesis conditions are associated with changes in crystal growth, particle aggregation, and microstructural features of the BiOI-based samples, while the major elemental constituents detected by EDX remain unchanged [7]. The combined EDX, SEM, and XRD results therefore indicate a relationship between the elemental composition, structural characteristics, and morphology of the synthesized samples. Overall, the results suggest that synthesis pH may influence the crystallite size, structural ordering, and morphological features of the green-synthesized BiOI-based materials.

3.4. Optical properties

3.4.1 UV-Vis Analysis

Fig. 6(a–d) shows the optical absorption spectra of the BiOI nanoparticles synthesized by maintaining pH 5,8,10,13 respectively obtained from LAMBDA 750 (Perkin Elmer) UV-vis NIR Spectrophotometer instrument. The materials exhibit a high absorbance level in the visible-light range, indicating the visible-light response of BiOI owing to its narrow band gap and layered tetragonal structure. A clear shift in the absorption edge based on the pH value of the

solution was observed, suggesting that the reaction pH value plays an important role in tuning the electronic structure and optical response of the synthesized nanoparticles. The absorption edges are determined to be 730, 532, 590, and 738 nm for the BiOI nanoparticles synthesized by maintaining pH values of 5, 8, 10, and 13, respectively, which correspond to an optical band gap energy of 1.69, 2.33, 2.10, and 1.67 eV, respectively, estimated from the absorption edges. The absorption-edge variation can be associated with the pH-dependent changes in crystallite characteristics and morphology, as synthesis conditions are known to influence the crystal growth, particle dimensions, and optical response of BiOI materials. At pH 5, the relatively large crystallite size of 25.30 ± 7.82 nm and highly agglomerated moss-rose/flower-like morphology are accompanied by a long-wavelength absorption edge at 730 nm. Such morphology-dependent optical variation is consistent with reports showing that different BiOI morphologies can exhibit different visible-light absorption and band-gap characteristics [6,7, 41]. At pH 8, the crystallite size decreases to 18.67 ± 4.86 nm and the morphology changes to hierarchical cauliflower-like microspheres composed of interconnected ultrathin nanosheets, accompanied by a pronounced blue shift of the absorption edge to 532 nm. The smaller crystallite dimensions and altered nanosheet-based architecture can modify the electronic and optical response through changes in crystal growth, surface structure, and defect/surface-state characteristics [41]. At pH 10, the slight increase in crystallite size to 20.37 ± 4.86 nm together with the development of interconnected rod-like crystallites and plate-like architectures is associated with an intermediate absorption edge of 590 nm. This further supports the influence of morphology and crystallite characteristics on the optical response of BiOI [41]. At pH 13, the crystallite size increases to 30.37 ± 11.34 nm, while densely agglomerated plate/sheet-like structures with elongated rod-like crystallites and the formation of the Bi_5O_7I phase are observed. The corresponding red shift to 738 nm and lower estimated band gap of 1.67 eV can therefore be associated with the combined influence of crystal growth, morphology, and phase evolution rather than crystallite size alone [7,41]. The overall trends observed in the UV–Vis spectra, XRD analysis, and SEM morphology therefore show consistent pH-dependent variations in the optical, structural, and morphological characteristics of the materials. However, these observations alone do not establish a direct causal relationship between crystallite size or morphology and the observed optical response. Instead, the variations are reasonably considered to reflect the combined influence of crystallite characteristics, morphology, and phase evolution induced by the synthesis pH.

3.4.2 Optical Band Gap Analysis using Tauc Plot

A Tauc plot is a graphical method used to determine the optical bandgap (Eg) of a material from UV–Vis absorption data. This provides important information regarding the electronic band structure and optical transition behavior of semiconductor nanomaterials. Tauc plots of $(\alpha h\nu)^{1/2}$ versus photon energy (E) and $(\alpha h\nu)^2$ versus photon energy (E) are shown in Figure.7 & Figure. 8 for BiOI nanoparticles prepared by maintaining (a)pH 5, (b) pH 8, (c) pH 10, and (d) pH 13. This is especially important for semiconductors, such as BiOI nanoparticles. The relationship used in the Tauc plot is as follows:

$$(\boldsymbol{\alpha h}\upsilon)^{\boldsymbol{n}} = \boldsymbol{A}\left(\boldsymbol{h}\upsilon - \boldsymbol{E_g}\right)$$

where α is the absorption coefficient, $\boldsymbol{h}\upsilon$ is the photon energy, A is a proportionality constant, and E_g is the optical bandgap energy.

In the present study, the UV–Vis absorption spectra were recorded using aqueous dispersions of the synthesized BiOI nanoparticles in distilled water. The absorption coefficient (α) was calculated from the measured absorbance using the relation $\alpha = 2.303A/t$, where A is the absorbance and t (=1 cm) is the optical path length of the cuvette. The photon energy was calculated from the wavelength using $h\nu = 1240/\lambda$, where λ is the wavelength in nm. For the Tauc analysis, $(\alpha h\nu)^{1/2}$ versus E (=hν) was used to estimate the indirect allowed transition, whereas $(\alpha h\nu)^2$ versus E (=hν) was used to estimate the direct allowed transition. The linear portions of the respective Tauc plots were selected and fitted by linear regression, and the optical bandgap was determined from the extrapolated intercept of the linear fit with the

photon-energy axis. The goodness of the linear fitting was evaluated using the coefficient of determination (R^2). In addition to the regression-based values, the band gaps were also estimated graphically by drawing a tangent/extrapolated line through the linear portion of each Tauc plot and determining its intercept with the photon-energy axis. Apparent optical transition energies obtained from linear regression and graphical tangent extrapolation, together with the coefficients of determination (R^2) and linear fitting ranges for BiOI nanoparticles synthesized at different pH values are listed in Table.4.

To gain insight into the electronic transitions, the optical band gaps of the BiOI nanoparticles were calculated based on the Tauc relation. The indirect-allowed and direct-allowed Tauc models were evaluated using the $(\alpha h\nu)^{1/2}$ versus photon energy (E) plots [Fig. 7(a–d)] and $(\alpha h\nu)^2$ versus photon energy (E) plots [Fig. 8(a–d)] respectively. The apparent optical transition energies obtained from linear regression and graphical tangent extrapolation are summarized in Table 3. In general, the regression-derived values were in close agreement with the corresponding graphical tangent values, indicating consistent estimation of the apparent optical transition energies. The fitting regions were selected from the approximately linear portions of the respective Tauc plots, and the corresponding regression coefficients (R^2) are also provided in Table 4. The fitted regions showed high linearity, supporting the reliability of the comparative analysis. The apparent indirect-allowed transition energy increased from pH 5 to pH 8 and subsequently decreased at pH 10 and pH 13. A similar trend was observed for the direct-allowed transition energy, with the highest value obtained for the pH 8 sample. These results indicate that the optical transition energies vary systematically with the synthesis conditions; however, the Tauc analysis alone does not establish the simultaneous occurrence of direct and indirect electronic transitions. Therefore, the values obtained from the two transition models are considered apparent optical transition energies and are used primarily for comparative analysis.

The graphical tangent method yielded indirect-transition energies of approximately 1.65, 2.23, 1.82, and 1.69 eV and direct-transition energies of approximately 2.20, 2.54, 2.41, and 2.29 eV for the samples synthesized at pH 5, 8, 10, and 13, respectively. The corresponding regression-derived direct-transition energies were approximately 2.170 ± 0.012, 2.523 ± 0.009, 2.404 ± 0.017, and 2.234 ± 0.008 eV, while the indirect-transition energies were approximately 1.607 ± 0.005, 2.202 ± 0.011, 1.759 ± 0.007, and 1.626 ± 0.006 eV, respectively. The small differences between the graphical tangent and regression-derived values can arise from the selection of the linear fitting region and the graphical extrapolation of the fitted region to the photon-energy axis. Nevertheless, both approaches show a similar overall variation in the apparent optical transition energies with synthesis pH, with the highest values observed for the pH 8 sample. For quantitative comparison, the regression-derived values and their associated uncertainties were used, while the graphical tangent values are presented as a visual representation of the extrapolated optical absorption edge.

For the BiOI samples synthesized at pH 5, 8, and 10, the indirect-transition model was considered the primary model for estimating the fundamental optical absorption edge, consistent with previous reports describing BiOI as an indirect-band-gap semiconductor with reported experimental values generally in the range of ~1.8–2.0 eV [42–43]. The direct-transition model was additionally evaluated because direct optical transitions have also been reported to contribute to the optical absorption of BiOI [42–44]; however, these values are considered complementary apparent transition energies rather than independent fundamental band gaps. The indirect-transition energies were 1.607 ± 0.005, 2.202 ± 0.011, and 1.759 ± 0.007 eV for pH 5, 8, and 10, respectively, while the corresponding direct-transition energies were 2.170 ± 0.012, 2.523 ± 0.009, and 2.404 ± 0.017 eV. At pH 13, the XRD results indicate the formation of Bi_5O_7I rather than pure BiOI; therefore, its optical response was considered separately. Bi_5O_7I has been reported as an indirect-band-gap semiconductor with optical band-gap values of approximately 2.56–2.59 eV [44,45]. Since the obtained indirect value of 1.626 ± 0.006 eV is substantially lower than this reported range, it is treated as an apparent optical transition energy rather than the definitive fundamental band gap. Similarly, the direct-transition value of 2.234 ± 0.008 eV is considered a complementary apparent transition energy. These lower-energy features may be associated with structural disorder, defect-related states, surface states, or other contributions to the absorption response under strongly alkaline conditions [47,48]. Thus, the Tauc analysis is primarily used here to compare the optical absorption-edge behavior of the samples rather than to establish simultaneous direct and indirect fundamental transitions. The

variation in the apparent transition energies with synthesis pH may reflect changes in phase composition, crystallinity, morphology, defects, and surface-related states [24,46–48].

3.5. Surface Charge and Colloidal Analysis

3.5.1 Zeta Potential Analysis

The high negative zeta potentials observed for the synthesized BiOI nanoparticles at different pH conditions have an obvious impact on the binding of the BiOI nanoparticle surface with polar water molecules during the air-to-water process [49]. The zeta potential measurements were carried out using a Zetasizer Nano ZSP (ZEN5600, Malvern Panalytical, UK) at the Central Instrumentation Facility, Malaviya National Institute of Technology (MNIT), Jaipur, India. Zeta potential measurements were performed for the green-synthesized BiOI nanoparticles to identify their surface charge and colloidal stability, as depicted in Fig. 9(a-d). The zeta potential measurements and corresponding statistical values are summarized in Table 5. The zeta potentials of the BiOI nanoparticles synthesized at pH 5, 8, 10, and 13 were -30.93 ± 1.61, -38.03 ± 0.24, -38.40 ± 1.56, and -40.83 ± 0.34 mV, respectively. All the samples possessed negative zeta potential values in the range higher than -30 mV, which explains that they are highly dispersed and exhibit great stability with electrostatic repulsive forces within the particles [47]. The higher the negative zeta potential with increasing pH, the more the pH of the solution affects the nature of the surface chemistry and mechanism for the stabilization of BiOI nanoparticles [49]. For example, with a comparatively low value of negative zeta potential of -30.93 ± 1.61 mV of BiOI synthesize by maintaining pH 5, we anticipate some extent of protonation on the phytochemical functional groups of curry leaf extracts and surface hydroxyl groups of BiOI NPs. Moreover, under acidic conditions. Higher amounts of H^+ ions lead to a decrease in the density of negative charges on the surfaces, thus resulting in weak inter-particle repulsive forces. These findings correlate positively with the SEM results, where highly packed clusters in cauliflower morphology suggest that particle aggregation prevails at low values of the surface charge. In addition, owing to the relatively weak crystallinity and high number of defects at acidic pH, as confirmed by the XRD data, rapid nuclei formation with a passive surface film of immature size could reduce colloidal stability [50].

Upon increasing synthesis pH to 8 and 10 further made the zeta potential negative more (-38.03 ± 0.24 and -38.40 ± 1.56 mV) which shows an increase in the adsorption of hydroxide ions on the surface as well as increase in deprotonation of oxygen-containing surface functional group of the nanoparticles. More numbers of negatively charged surface sites will result in a larger repulsive force preventing particles from agglomerating, which in turn resulted in better dispersed morphological flower-like morphology and interconnected nanosheets with less aggregation (fig. 2a and b), which are corroborated well with our above interpretation. Simultaneously, XRD indicates enhanced crystallinity, fewer lattice defects, and greater structural ordering of the nanoparticles formed with optimum pH conditions under a moderately alkaline medium, which is favorable for preparing well-ordered structures and well-dispersed colloidally stable BiOI nanoparticles. A higher negative surface charge enhances the electrostatic attraction of polar molecules to the nanoparticle surface, which is advantageous for applications such as photocatalysis, environmental remediation, and atmospheric water harvesting. The highest negative zeta potential (-40.83 ± 0.34 mV) obtained for the sample synthesized at pH 13 indicates excellent colloidal stability arising from strong electrostatic repulsion between the suspended nanoparticles [50]. Under strongly alkaline conditions, the increased concentration of OH^- ions promote the deprotonation of surface hydroxyl groups, resulting in a higher density of negatively charged surface species. This behavior is consistent with the enhanced hydrophilicity observed from contact-angle measurements and the morphological evolution revealed by SEM. Although the XRD results indicate an increase in crystallite size and the SEM images show the formation of densely aggregated plate-like and sheet-like structures, the nanoparticles retain high suspension stability because the surface electrostatic repulsion effectively counterbalances the tendency for particle aggregation in dispersion. Therefore, the present results suggest that while the hydrothermal

synthesis conditions strongly influence crystal growth and morphology, the colloidal stability of BiOI nanoparticles is predominantly governed by their surface charge characteristics and electrostatic interactions [49–50].

The progressive increase in the negative zeta potential with increasing synthesis pH is consistent with the FTIR results, which reveal a broad O–H stretching band associated with surface hydroxyl groups and oxygen-containing phytochemical constituents derived from the curry leaf extract. These functional groups are likely to participate in the surface functionalization of BiOI nanoparticles during hydrothermal synthesis, thereby contributing to the development of a more negatively charged surface and improved colloidal stability through enhanced electrostatic repulsion between the nanoparticles. The combined FTIR and zeta potential analyses therefore highlight the dual role of the curry leaf phytochemicals as natural reducing and surface-capping agents, enabling the formation of stable BiOI nanoparticles without the use of synthetic surfactants or polymeric stabilizers. The increasingly negative surface charge is expected to enhance the adsorption of positively charged species and improve interfacial interactions, which may be advantageous for surface-dependent processes such as photocatalysis, environmental remediation, and atmospheric water harvesting. Furthermore, the high negative zeta potential (up to -40.83 ± 0.34 mV) confirms excellent suspension stability, ensuring a well-dispersed colloidal system that is desirable for subsequent functional and catalytic applications.

3.6 Surface Wettability and Hydrophilicity

3.6.1 Contact Angle Measurements

The water contact angle of the synthesized BiOI nanoparticles was measured using a Drop Shape Analyzer (DSA 25) goniometer (KRUSS GmbH, Hamburg, Germany) at the Centre for Nanoscience, Indian Institute of Technology (IIT) Kanpur, India. To test the surface wettability of the BiOI nanoparticles green-synthesized**,** water contact angle was measured at two different locations on each BiOI-coated glass substrate. At each location, the contact angles obtained from the left and right sides of the water droplet were averaged to obtain a location-specific contact angle. The mean contact angle and standard deviation (SD) were subsequently calculated from the two location-specific average values and reported as mean ± SD. Representative water contact angle images corresponding to the measured values closest to the calculated mean ± standard deviation were selected for presentation. The representative images for the BiOI samples synthesized at pH 5, 8, 10, and 13 are shown in Figure 10(a–d)**,** respectively. The water contact-angle measurements and corresponding statistical values are summarized in Table 6.

The water contact angle (WCA) decreased systematically from 53.57 ± 2.23° for pH 5 to 43.47 ± 1.52°, 31.57 ± 2.29°, and 23.03 ± 2.29° for pH 8, 10, and 13, respectively, indicating progressively enhanced surface wettability. At pH 5, the relatively large crystallite size (25.30 ± 7.82 nm) and highly agglomerated moss-rose/flower-like microspheres observed by SEM provide a comparatively less accessible surface for water spreading, resulting in the highest WCA. With increasing pH to 8 and 10, the crystallite size decreased to 18.67 ± 4.86 and 20.37 ± 4.86 nm, respectively, while the morphology evolved into hierarchical nanosheet- and interconnected rod/plate-like structures, which can increase the effective surface area and facilitate water spreading [51,52]. The further decrease in WCA to 23.03 ± 2.29° at pH 13, despite the increase in crystallite size to 30.37 ± 11.34 nm and formation of densely packed plate/sheet-like Bi5O7I structures, indicates that crystallite size alone does not control wettability; rather, the morphology, surface topography, and phase-dependent surface characteristics collectively contribute to the observed hydrophilicity [52,53]. For rough hydrophilic surfaces, increased surface texture can enhance apparent wettability by increasing the effective solid–liquid interaction area, consistent with the Wenzel wetting model [53].

The consistent trends observed in XRD, SEM, FTIR, zeta potential, and water contact-angle measurements demonstrate that synthesis pH governs the structure–morphology–surface characteristics of the green-synthesized BiOI/Bi_5O_7I materials. The progressive decrease in contact angle from 53.57 ± 2.23° to 23.03 ± 2.29° indicates

enhanced surface wettability with increasing synthesis pH, which is associated with the pH-dependent evolution of crystallite structure, hierarchical morphology, and surface chemical characteristics [50–53]. Such hydrophilic surfaces can promote water spreading and facilitate the removal of surface contaminants, providing potential for self-cleaning coatings [53-55]. In practical applications, wettability-controlled self-cleaning coatings have been investigated for glass windows, building surfaces, vehicle glazing, photovoltaic panels, and other exposed surfaces where reduced dust and contaminant accumulation is desirable [53-57]. Therefore, the pH-controlled BiOI/Bi_5O_7I system provides a promising basis for designing functional surfaces with tunable wetting behavior, although dedicated self-cleaning and durability tests would be required to establish its practical performance.

4. Conclusion

In this study, BiOI/Bi_5O_7I nanoparticles were synthesized through a green hydrothermal route using Murraya koenigii (curry leaf) extract at reaction pH values of 5, 8, 10, and 13. The results show that synthesis pH has a substantial influence on the structural, morphological, optical, and interfacial characteristics of the resulting materials. XRD analysis indicated that the samples prepared at pH 5, 8, and 10 retained the tetragonal BiOI structure, whereas a structural transformation toward an orthorhombic phase was observed under strongly alkaline conditions at pH 13. Changes in crystallite size, crystallinity, lattice strain, and defect-related parameters were also observed with variation in synthesis pH. The highest crystallinity (95.37%) and crystallite size (30.37±11.34 nm) were obtained for the pH 13 sample, indicating enhanced crystal growth under strongly alkaline conditions. FTIR analysis identified characteristic vibrational features associated with the bismuth oxyiodide framework and surface functional groups. The possible contribution of plant-derived species to surface stabilization is considered in the context of the green synthesis route, although their specific chemical identity and surface binding require further investigation. SEM analysis revealed clear morphological changes with increasing pH, from cauliflower-like and hierarchical flower-like structures at pH 5 and 8 to interconnected rod-like assemblies at pH 10 and densely aggregated plate- and sheet-like structures decorated with fine crystallites at pH 13. These morphological variations were accompanied by the structural changes observed by XRD, indicating that solution chemistry plays an important role in crystal growth and microstructural development. EDX analysis confirmed Bi, O, and I as the principal constituent elements in the investigated samples, while the relative elemental composition showed no major change sufficient to account for all of the observed morphological variations. UV–Vis measurements showed changes in the absorption behaviour with variation in synthesis pH. Tauc analysis provided estimated indirect band-gap values of 1.607 ± 0.005, 2.202 ± 0.011, 1.759 ± 0.007, and 1.626 ± 0.006 eV and direct-transition estimates of 2.170 ± 0.012, 2.523 ± 0.009, 2.404 ± 0.017, and 2.234 ± 0.008 eV for the samples prepared at pH 5, 8, 10, and 13, respectively. These values indicate variations in the optical response with synthesis conditions; however, the Tauc-derived values should be regarded as estimates associated with the selected transition models rather than definitive evidence for simultaneous direct and indirect electronic transitions. The variation in optical band-gap values may be associated with changes in crystallinity, crystallite size, structural disorder, and local structural environment. Further optical and electronic-structure investigations would be required to establish the underlying mechanisms more conclusively.

Surface characterization also demonstrated pH-dependent changes in the interfacial properties. The zeta potential became progressively more negative, reaching −40.83 ± 0.34 mV for the pH 13 sample, suggesting increased electrostatic repulsion and improved colloidal stability under the measurement conditions. The water contact angle decreased from 53.57 ± 2.23° to 23.03 ± 2.29°, indicating a substantial increase in surface wettability with increasing synthesis pH. These changes demonstrate that synthesis pH can influence not only the bulk structural characteristics but also the surface properties of the resulting materials. The main contribution of the present study is the integrated experimental comparison of pH-dependent structural, morphological, optical, surface-charge, and wettability changes in plant-assisted hydrothermally synthesized bismuth oxyiodide materials. Rather than considering pH-dependent structural evolution as a new phenomenon, this work examines how several experimentally measured properties vary together under the selected green synthesis conditions. In particular, the observed tetragonal-to-orthorhombic

structural transformation at strongly alkaline pH, together with the accompanying morphological and interfacial changes, provides a useful basis for understanding the influence of synthesis conditions on these materials.

Among the investigated conditions, the sample prepared at pH 8 showed well-developed hierarchical morphology and high structural ordering, whereas the pH 13 sample exhibited the largest crystallite size, highest negative zeta potential, and lowest contact angle among the investigated samples. These differences demonstrate that the preferred synthesis condition may depend on the specific property of interest. However, the present study does not directly evaluate photocatalytic, photo-electrochemical, optoelectronic, self-cleaning, antibacterial, or atmospheric water-harvesting performance. Therefore, the observed structural, optical, and surface characteristics may provide a basis for future application-oriented investigations, but further experiments are required to establish the suitability of these materials for such applications. Overall, the study demonstrates that reaction pH is a useful processing parameter for modifying the physicochemical characteristics of plant-assisted bismuth oxyiodide materials and provides a comparative basis for their further investigation.

References

1. Matthew N. Gordon, Kaustav Chatterjee, Nayana Christudas Beena, Sara E. Skrabalak; Sustainable Production of Layered Bismuth Oxyhalides for Photocatalytic H_2 Production. *ACS Sustainable Chem. Eng.* 5 December 2022; 10 (48): 15622–15641. https://doi.org/10.1021/acssuschemeng.2c05326
2. Zhang, X., & Zhang, L. (2010). Electronic and Band Structure Tuning of Ternary Semiconductor Photocatalysts by Self Doping: The Case of BiOI. The Journal of Physical Chemistry C, 114(42), 18198–18206. https://doi.org/10.1021/jp105118m
3. Li, Y., Wang, J., Yao, H., Dang, L. and Li, Z. (2011) Efficient Decomposition of Organic Compounds and Reaction Mechanism with BiOI Photocatalyst under Visible Light Irradiation. Journal of Molecular Catalysis A: Chemical, 334, 116-122. https://doi.org/10.1016/j.molcata.2010.11.005
4. Sun, Z., & Amrillah, T. (2024). Potential application of bismuth oxyiodide (BiOI) when it meets light. *Nanoscale*, *16*(10), 5079–5106. https://doi.org/10.1039/d3nr06559f
5. Malathi Arumugam, Myong Yong Choi, Recent progress on bismuth oxyiodide (BiOI) photocatalyst for environmental remediation, Journal of Industrial and Engineering Chemistry, Volume 81,2020, Pages 237-268, https://doi.org/10.1016/j.jiec.2019.09.013.
6. Hu J, Weng S, Zheng Z, Pei Z, Huang M, Liu P (2014) Solvents mediated synthesis of BiOI photocatalysts with tunable morphologies and their visible-light driven photocatalytic performances in removing of arsenic from water. J Hazard Mater 264:293–302, https://doi.org/10.1016/j.jhazmat.2013.11.027
7. Long Y, Wang Y, Zhang D, Ju P, Sun Y (2016) Facile synthesis of BiOI in hierarchical nanostructure preparation and its photocatalytic application to organic dye removal and biocidal effect of bacteria. J Colloid Interface Sci 481:47–56, https://doi.org/10.1016/j.cej.2016.01.032
8. Xiao X, Zhang W-D (2010) Facile synthesis of nanostructured BiOI micro spheres with high visible light-induced photocatalytic activity; Journal of Material Chemistry 20(28):5866–5870, https://doi.org/10.1039/C0JM00333F
9. Mera AC, Rodríguez C, Meléndrez M, Valdés H (2017) Synthesis and characterization of BiOI microspheres under standardized conditions. J Mater Sci 52:944–954, https://doi.org/10.1007/s10853-016-0390-x
10. G. Mohan Kumar, Deepak Suresh Varma, Dr. Sathiskumar Jothi, Dr. Devaraj Ramasamy, Dr. João C. C. Abrantes, Dr. Murali Rangarajan, pH-Dependent Synthesis of Pure-Phase BiI_3 and BiOI by Electrodeposition, ChemistrySelect 2023, 8, e202302055, https://doi.org/10.1002/slct.202302055
11. Martinez-Topete, A., Jimenez-Relinque, E., Dappozze, F. *et al.* Bismuth oxyiodides: photocatalytic performance, by-products, and degradation pathways. *J Mater. Sci: Mater Eng.* **20**, 39 (2025). https://doi.org/10.1186/s40712-025-00251-6
12. Syed, S.M., Kulkarni, S., Patil, M. *et al.* A comprehensive review of green synthesis methods and applications of nanoparticles derived from plant extracts and microorganisms. *Discov. Green Chem.* **1**, 6 (2026). https://doi.org/10.1007/s44509-026-00006-2
13. Jun Di, Jiexiang Xia, Mengxia Ji, Bin Wang, Sheng Yin, Qi Zhang, Zhigang Chen, Huaming Li; Carbon Quantum Dots Modified BiOCl Ultrathin Nanosheets with Enhanced Molecular Oxygen Activation Ability for Broad Spectrum Photocatalytic Properties and Mechanism Insight. *ACS Appl. Mater. Interfaces* 16 September 2015; 7 (36): 20111–20123. https://doi.org/10.1021/acsami.5b05268
14. Xin Xiao, Wei-De Zhang; Facile synthesis of nanostructured BiOI microspheres with high visible light-induced photocatalytic activity. *J. Mater. Chem.* 2010; 20 (28): 5866–5870. https://doi.org/10.1039/c0jm00333f
15. Yongchao Huang, Haibo Li, Muhammad-Sadeeq Balogun, Wenyue Liu, Yexiang Tong, Xihong Lu, Hongbing Ji; Oxygen Vacancy Induced Bismuth Oxyiodide with Remarkably Increased Visible-Light Absorption and Superior Photocatalytic Performance. *ACS Appl. Mater. Interfaces* 24 December 2014; 6 (24): 22920–22927. https://doi.org/10.1021/am507641k
16. Shuaihong Chen, Xinmin Wei, Xilun Wang, Chunli Jiang, Yong Jiang; Oxygen Vacancy-Rich Bi_2WO_6-Monolayered Nanosheets Boost Solar-Driven Photocatalytic-Selective Oxidation of 5-Hydroxymethylfurfural to 2,5-Diformylfuran. *Ind. Eng. Chem. Res.* 18 June 2025; 64 (24): 11724–11732. https://doi.org/10.1021/acs.iecr.5c00530
17. Mehwish Tabassum, Aima-tul-ayesha, Bin Yang, Xin Jia, Muhammad Nadeem Zafar, Progress on synthesis, characterization and photocatalytic applications of bismuth oxyhalide based nanomaterials in cleaner

environment and energy - A review, Journal of Cleaner Production, Volume 494, 2025, 144868, https://doi.org/10.1016/j.jclepro.2025.144868.
18. Yunan Wang, Kejian Deng, Lizhi Zhang; Visible Light Photocatalysis of BiOI and Its Photocatalytic Activity Enhancement by in Situ Ionic Liquid Modification. *J. Phys. Chem. C* 28 July 2011; 115 (29): 14300–14308. https://doi.org/10.1021/jp2042069
19. Xin Xiao, Rong Hao, Min Liang, Xiaoxi Zuo, Junmin Nan, Laisheng Li, Weide Zhang, One-pot solvothermal synthesis of three-dimensional (3D) BiOI/BiOCl composites with enhanced visible-light photocatalytic activities for the degradation of bisphenol-A, Journal of Hazardous Materials, Volumes 233–234, 2012, Pages 122-130, https://doi.org/10.1016/j.jhazmat.2012.06.062.
20. Akihiko Kudo, Yugo Miseki; Heterogeneous photocatalyst materials for water splitting. *Chem. Soc. Rev.* 2009; 38 (1): 253–278. https://doi.org/10.1039/b800489g
21. Akira Fujishima, Xintong Zhang, Donald A. Tryk, TiO_2 photocatalysis and related surface phenomena, Surface Science Reports, Volume 63, Issue 12, 2008, Pages 515-582, https://doi.org/10.1016/j.surfrep.2008.10.001.
22. Irshad Ahmad, Yanhong Zou, Jiaying Yan, Yuyu Liu, Shazia Shukrullah, Muhammad Yasin Naz, Humaira Hussain, Waheed Qamar Khan, N.R. Khalid, Semiconductor photocatalysts: A critical review highlighting the various strategies to boost the photocatalytic performances for diverse applications, Advances in Colloid and Interface Science, Volume 311, 2023, 102830, https://doi.org/10.1016/j.cis.2022.102830.
23. [23] Md. Ashraful Alam, Shanawaz Ahmed, Raton Kumar Bishwas, Sabrina Mostofa, Shirin Akter Jahan, X-ray crystallographic diffraction study by whole powder pattern fitting (WPPF) method: Refinement of crystalline nanostructure polymorphs TiO_2 ,South African Journal of Chemical Engineering, Volume 51, January 2025, Pages 68-77, https://doi.org/10.1016/j.sajce.2024.10.010
24. Aleksei I. Noskov, Alexander B. Kotlyar, Liat Katrivas, Zakhar Reveguk, Evan P. Garcia, V. Ara Apkarian, Christophe Galland, Eric O. Potma, Dmitry A. Fishman; Overcoming the Indirect Band Gap: Efficient Silicon Emission via Momentum-Engineered Photonic States. *Nano Lett.* 22 April 2026; 26 (15): 5187–5194. https://doi.org/10.1021/acs.nanolett.6c00596
25. Aynun Nahar, Md. Sahadat Hossain, Md. Ahedul Akbor, Subarna Sandhani Dey, Md. Ashraful Alam, Sharmin Ahmed Trisha, Tania Afrose Sheoly, Nigar Sultana Pinky, Farhana Afrose Sonia, Evaluation of anti-microbial activity of biotite and biotite composite based on crystallographic parameters: Estimation of crystallite size employing X-ray diffraction data, Results in Engineering, Volume 23, 2024, 102595, https://doi.org/10.1016/j.rineng.2024.102595.
26. Quan-Cheng Liu, De-Kun Ma, Ying-Ying Hu, Ya-Wen Zeng, and Shao-Ming Huang; Various Bismuth Oxyiodide Hierarchical Architectures: Alcohothermal-Controlled Synthesis, Photocatalytic Activities, and Adsorption Capabilities for Phosphate in Water, ACS Appl. Mater. Interfaces 2013, 5, 11927−11934, https://doi.org/10.1021/am4036702
27. Limin Song, Shujuan Zhang, Qingwu Wei; Porous BiOI Sonocatalysts: Hydrothermal Synthesis, Characterization, Sonocatalytic, and Kinetic Properties. *Ind. Eng. Chem. Res.* 25 January 2012; 51 (3): 1193–1197. https://doi.org/10.1021/ie201753a
28. Kashif, M., Gul, M., Shahzad, N., Sun, H., Shezan, S. A., Ahmad, N., Hamlaoui, O., & Tozan, H. (2026). Metal Oxide Nanoparticles: A Comprehensive Review of Recent Advances in Synthesis Strategies, Characterization and Multifunctional Applications. *Catalysts*, *16*(8), 678. https://doi.org/10.3390/catal16080678
29. Xu Yana, Long Pana, Yanli Maoa, Haiyan Kanga, Zhongxian Songa, Xia Zhanga, Xiaole Yana, Wei Mab, Biao Liua, Yong Zhao; Carbon quantum dots decorated $Bi_4O_5I_2$ with greatly improved visible-light photocatalytic performance, Desalination and Water Treatment, 230 (2021) 411–418, 10.5004/dwt.2021.27431
30. Klimm, D. (2017). Thermodynamic and Kinetic Aspects of Crystal Growth. In Handbook of Solid State Chemistry (eds R. Dronskowski, S. Kikkawa and A. Stein). https://doi.org/10.1002/9783527691036.hsscvol2022
31. I.M. Lifshitz, V.V. Slyozov, The kinetics of precipitation from supersaturated solid solutions, Journal of Physics and Chemistry of Solids, Volume 19, Issues 1–2, 1961, Pages 35-50, https://doi.org/10.1016/0022-3697(61)90054-3.

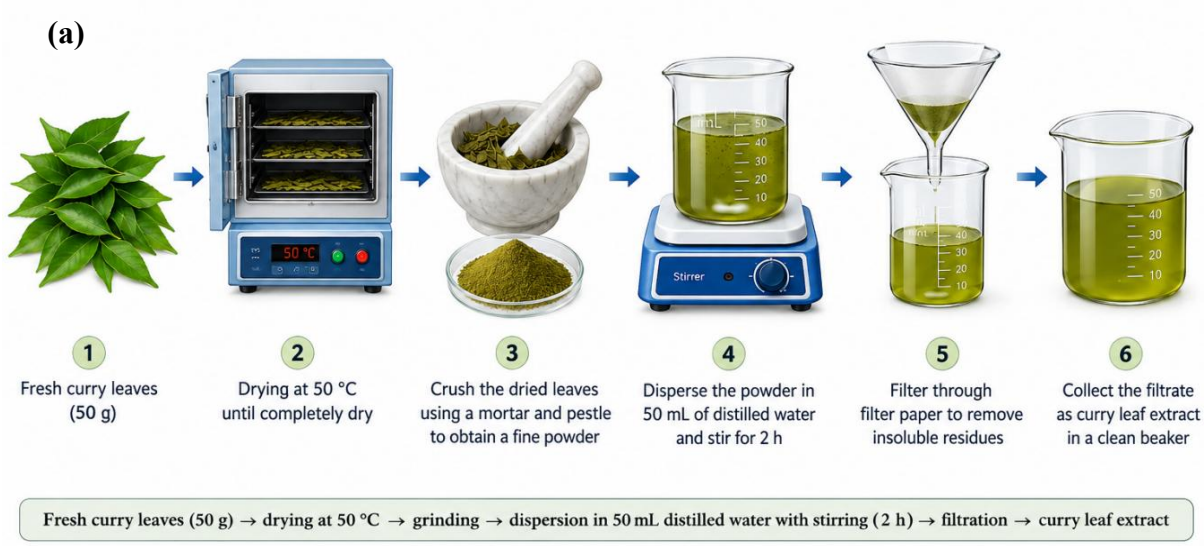
32. Gongjuan Wu, Yan Zhao, Yawen Li, Hongmei Ma, Jingzhe Zhao; pH-dependent synthesis of iodine-deficient bismuth oxyiodide microstructures: Visible-light photocatalytic activity, Journal of Colloid and Interface Science 510 (2018) 228–236, https://doi.org/10.1016/j.jcis.2017.09.053
33. Juheon Lee, Bong-Ki Min, Insu Cho, and Youngku Sohn; Synthesis and Characterization of 1-D BiSI and 2-D BiOI Nanostructures, Bull. Korean Chem. Soc. 2013, Vol. 34, No. 3 773 doi: http://dx.doi.org/10.5012/bkcs.2013.34.3.773
34. Mengwei Li, Shangzhen Xie**,** Guangyi Tian, Guopeng Chen, Zhiguang Guo**;** Biomimetic Leaf-Shaped Wedge Structure with Mixed Wettability for Fog Harvesting, ACS Applied Materials & Interfaces Vol 16/Issue 32, doi: https://pubs.acs.org/doi/10.1021/acsami.4c08254
35. Lu Xue, Yi Du, Xinyue Sun, Nan Jiang, Junnan Qu, Jinghong Zhao; Preparation of a $Bi_4O_5I_2/Bi_2O_2CO_3$ p-n heterojunction with enhanced photocatalytic degradation performance by a one-pot solvothermal method, Materials Science in Semiconductor Processing 141 (2022) 106447, https://doi.org/10.1016/j.mssp.2021.106447
36. Mahmoodi, V., Ahmadpour, A., Rohani Bastami, T. and Hamed Mousavian, M.T. (2018), Facile Synthesis of BiOI Nanoparticles at Room Temperature and Evaluation of their Photoactivity Under Sunlight Irradiation. Photochem Photobiol, 94: 4-16. https://doi.org/10.1111/php.12832
37. Yoganand Singh, Himanshu Patel , Ananya Rai, Sakshi Singh, Nikhil Srivastav, Pankaj Srivastava; Bio-capped synthesis of TiO2 nanoparticle using Murraya koenigii leaf extract via ultrasonication assisted sol-gel method and its advanced DSSC performance, Next Materials 8 (2025) 100680, doi: https://doi.org/10.1016/j.nxmate.2025.100680
38. Owais Mehraj, Bilal M. Pirzada, Niyaz A. Mir, Mohammad Zain Khan, Suhail Sabir, A highly efficient visible-light-driven novel p-n junction Fe2O3/BiOI photocatalyst: Surface decoration of BiOI nanosheets with Fe2O3 nanoparticles, Applied Surface Science, Volume 387, 2016, Pages 642-651, https://doi.org/10.1016/j.apsusc.2016.06.166.
39. Xia, J. X.; Yin, S.; Li, H. M.; Xu, H.; Yan, Y. S.; Zhang, Q. Self-Assembly and Enhanced Photocatalytic Properties of BiOI Hollow Microspheres via a Reactable Ionic Liquid ,Langmuir 2011, 27, 1200−1206; https://doi.org/10.1021/la104054r
40. Lv X, Lam FLY and Hu X (2022) A Review on Bismuth Oxyhalide (BiOX, X=Cl, Br, I) Based Photocatalysts for Wastewater Remediation. Front. Catal. 2:839072. doi: 10.3389/fctls.2022.839072
41. Avanish Mishra, Awantika Shahi, Satya Pal Singh, Shweta Agrahari; A predictive formalism based on chi-square fitting for size & shape dependent estimation of bandgaps of nanomaterials, Solid State Communications 404 (2025) 116056, doi: https://doi.org/10.1016/j.ssc.2025.116056
42. Roberto Altieri, Fabian Schmitz, Manuel Schenker, Felix Boll, Luca Rebecchi, Pascal Schweitzer, Matteo Crisci, Ilka Kriegel, Bernd Smarsly, Derck Schlettwein, Francesco Lamberti, Teresa Gatti, Mengjiao Wang; Development of an automated SILAR method for the sustainable fabrication of BiOI/TiO_2 photoanodes. *Energy Adv.* 2024; 3 (10): 2564–2574. https://doi.org/10.1039/d4ya00405a
43. Lal, S., Righetto, M., Ulatowski, A. M., Motti, S. G., Sun, Z., MacManus-Driscoll, J. L., Hoye, R. L. Z., & Herz, L. M. (2023). Bandlike Transport and Charge-Carrier Dynamics in BiOI Films. *The journal of physical chemistry letters*, *14*(29), 6620–6629. https://doi.org/10.1021/acs.jpclett.3c01520
44. Jagt, R.A., Bravić, I., Eyre, L. *et al.* Layered BiOI single crystals capable of detecting low dose rates of X-rays. *Nat Commun* **14**, 2452 (2023). https://doi.org/10.1038/s41467-023-38008-4
45. Yang Y, Lai M, Huang J, Li J, Gao R, Zhao Z, Song H, He J and Ma Y (2021) Bi5O7I/g-C3N4 Heterostructures With Enhanced Visible-Light Photocatalytic Performance for Degradation of Tetracycline Hydrochloride. Front. Chem. 9:781991. doi: 10.3389/fchem.2021.781991
46. Mingce Long, Peidong Hu, Haodong Wu, Yuanyuan Chen, Beihui Tan, Weimin Cai; Understanding the composition and electronic structure dependent photocatalytic performance of bismuth oxyiodides. J. Mater. Chem. A 2015; 3 (10): 5592–5598. https://doi.org/10.1039/c4ta06134a
47. Lin, J., Hu, Z., Li, H., Qu, J., Zhang, M., Liang, W., & Hu, S. (2019). Ultrathin Nanotubes of Bi_5O_7I with a Reduced Band Gap as a High-Performance Photocatalyst. *Inorganic chemistry*, *58*(15), 9833–9843. https://doi.org/10.1021/acs.inorgchem.9b00858
48. Jian Feng, Xia Ran, Yan Wang, Song Zhan, Li Wang, Bo Xiao, Yeshuang Zhong, Dingguo Xu, Guangwei Feng, Zeqin Dai; Modulation of surface oxygen vacancies on bismuth-rich Bi_5O_7I nanoparticles for efficiently boosting photocatalytic overall water splitting, Applied Surface Science, Volume 655, 2024, 159517, https://doi.org/10.1016/j.apsusc.2024.159517.

49. Serrano-Lotina, R. Portela, P. Baeza, V. Alcolea-Rodriguez, M. Villarroel, P. Ávila, Zeta potential as a tool for functional materials development, Catalysis Today, Volume 423, 2023, 113862, https://doi.org/10.1016/j.cattod.2022.08.004.
50. Dembek, M., Bocian, S., & Buszewski, B. (2022). Solvent Influence on Zeta Potential of Stationary Phase—Mobile Phase Interface. *Molecules*, *27*(3), 968. https://doi.org/10.3390/molecules27030968
51. Garg, S., Yadav, M., Chandra, A., Sapra, S., Gahlawat, S., Ingole, P. P., Pap, Z., & Hernadi, K. (2018). Biofabricated BiOI with enhanced photocatalytic activity under visible light irradiation. *RSC advances*, *8*(51), 29022–29030. https://doi.org/10.1039/c8ra05661g
52. Xin Zhang, Weiwei Yang, Manyi Gao, *et al.* Room-temperature solid phase surface engineering of BiOI sheets stacking g-C3N4 boosts photocatalytic reduction of Cr(VI)[J]. Green Energy & Environment, 2022, 7(1): 66-74. DOI: 10.1016/j.gee.2020.07.024.
53. Robert N. Wenzel; Surface Roughness and Contact Angle.. *J. Phys. Chem.* 1 September 1949; 53 (9): 1466–1467. https://doi.org/10.1021/j150474a015
54. Satya Pal Singh, Archana Kumari Singh ; Formation of trapped meta-stable liquid–vapour interfaces in polar liquids in presence of excess gas-like molecules: Anomalous heat capacities and emergence of microscopic bubbles, Results in Physics, Volume 50, July 2023, 106554, https://doi.org/10.1016/j.rinp.2023.106554
55. Singh, Satya Pal, Spinodal Theory: A Common Rupturing Mechanism in Spinodal Dewetting and Surface Directed Phase Separation (Some Technological Aspects: Spatial Correlations and the Significance of Dipole-Quadrupole Interaction in Spinodal Dewetting), Advances in Condensed Matter Physics, 2011, 526397, 14 pages, 2011. https://doi.org/10.1155/2011/526397
56. Suqi Xue, Shanglei Yang, Xiner Li, Qiubo Li, Bangguo Hu; A comprehensive review on self-cleaning glass surfaces: durability, mechanisms, and functional applications. *RSC Adv.* 2024; 14 (46): 34390–34414. https://doi.org/10.1039/d4ra06680d
57. Singh, S.P., Singh, J.K. & Sharma, A. Adsorption of gas-like molecules to self-aligned square-well fluid channels under confinement of chemically patterned substrates. *Appl Nanosci* 3, 179–187 (2013). https://doi.org/10.1007/s13204-012-0118-4

Data Availability: The data supporting the findings of this study are available from the corresponding author upon reasonable request.

Funding: The authors received no specific funding for this work from any public, commercial, or not-for-profit funding agency.

Figure 1(a). Schematic representation of the preparation of curry leaf extract from fresh curry leaves. (b) Schematic illustration of the synthesis route for $BiOI/Bi_5O_7I$ nanoparticles prepared by the green hydrothermal method while maintaining the reaction pH at 5, 8, 10, and 13.



(b) Schematic illustration of the synthesis route for $BiOI/Bi_5O_7I$ nanoparticles

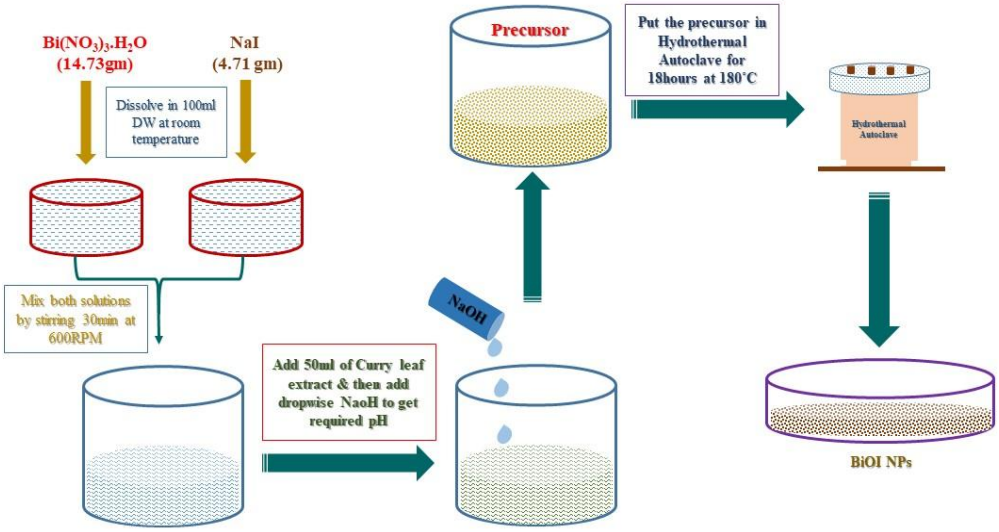


Figure 2. XRD patterns of BiOI nanoparticles synthesized at different pH conditions: (a) pH 5, (b) pH 8, (c) pH 10, and (d) pH 13.

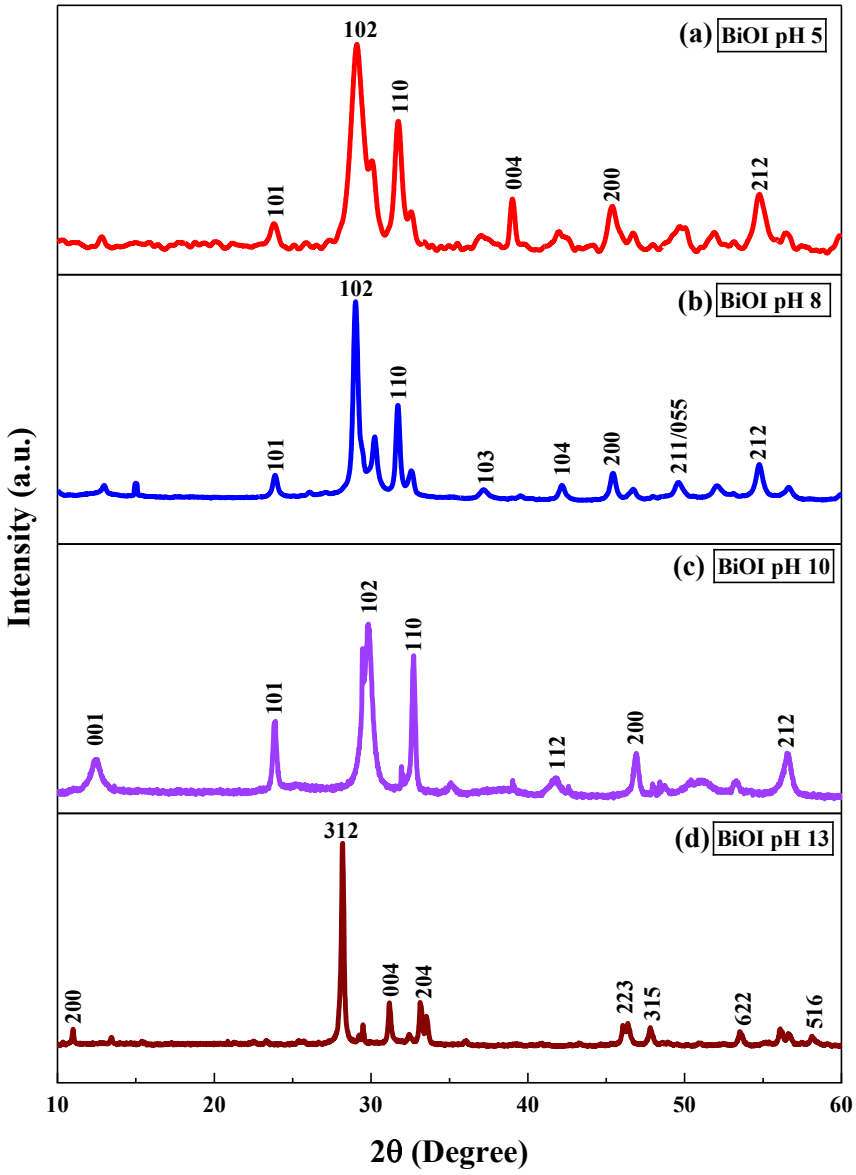
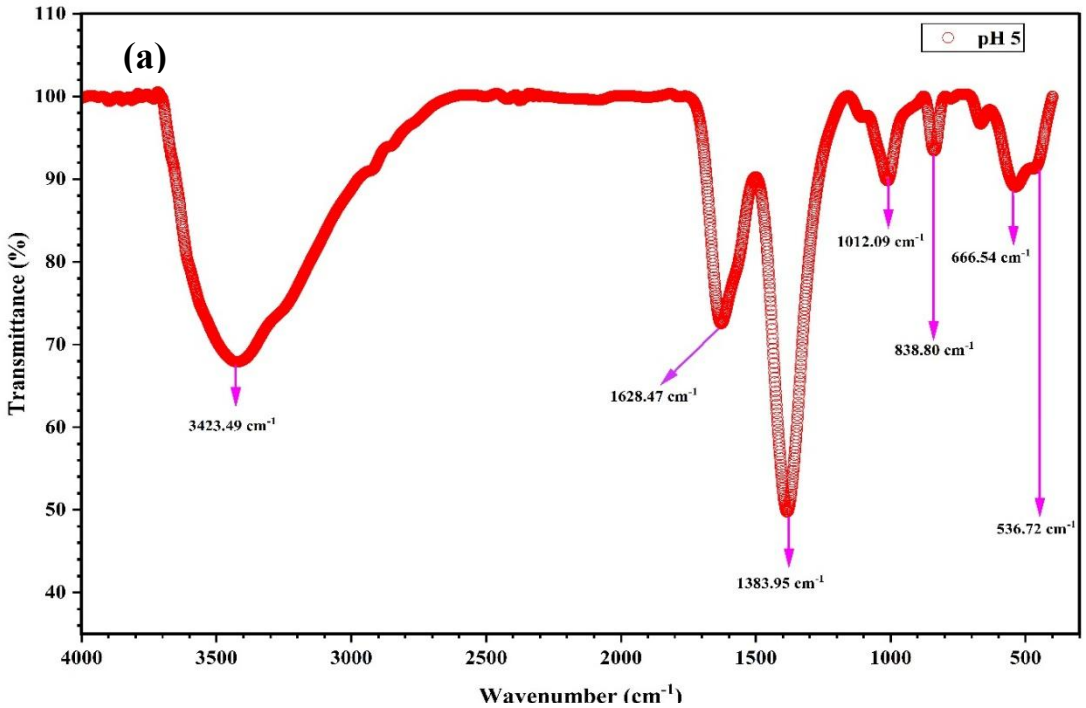
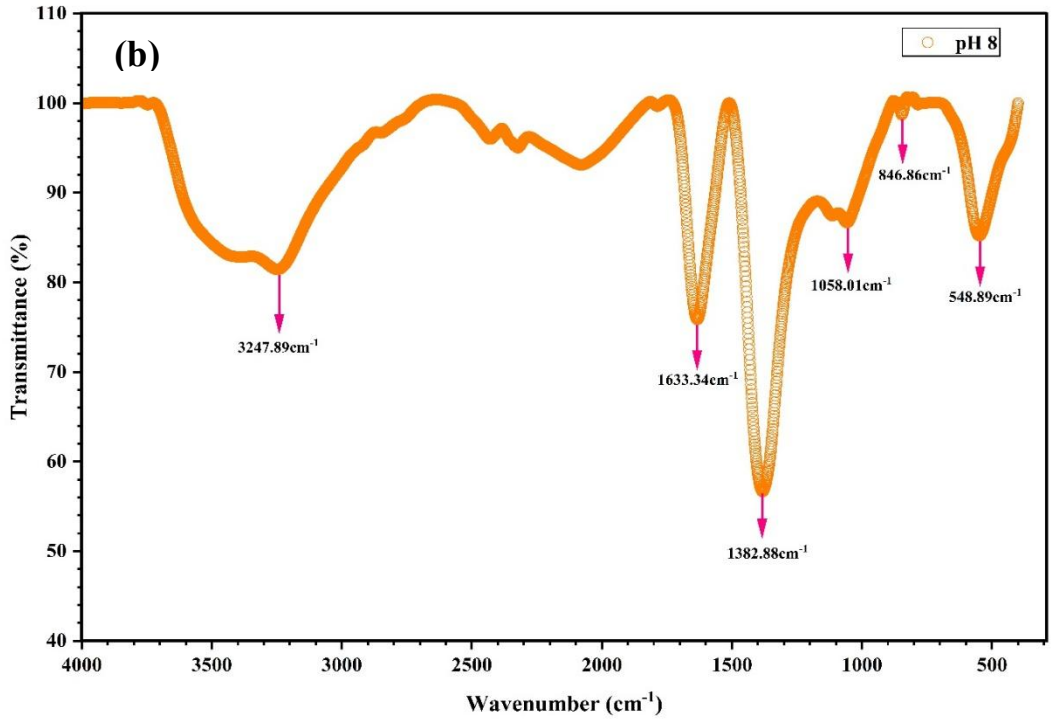
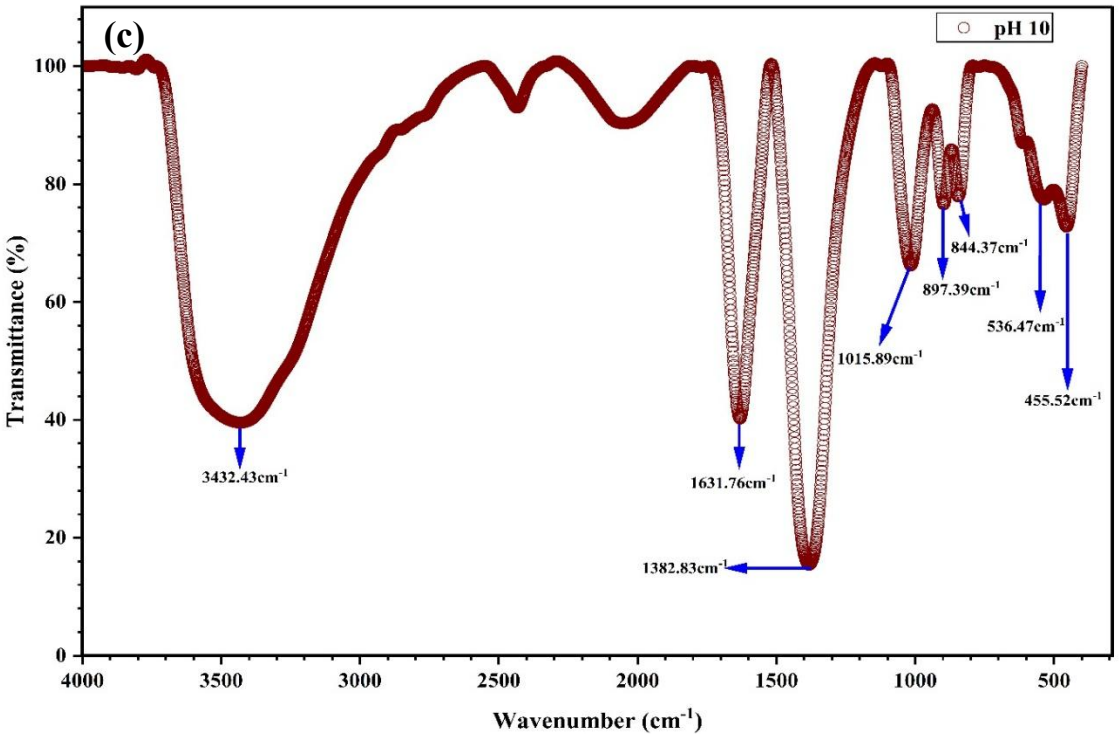


Figure 3. FTIR spectra of the BiOI nanoparticles synthesized by maintaining pH values of (a) pH 5, (b) pH 8, (c) pH 10, and (d) pH 13






(c)
pH 10
Transmittance (%)
Wavenumber (cm-1)
3432.43cm-1
1631.76cm-1
1382.83cm-1
1015.89cm-1
897.39cm-1
844.37cm-1
536.47cm-1
455.52cm-1

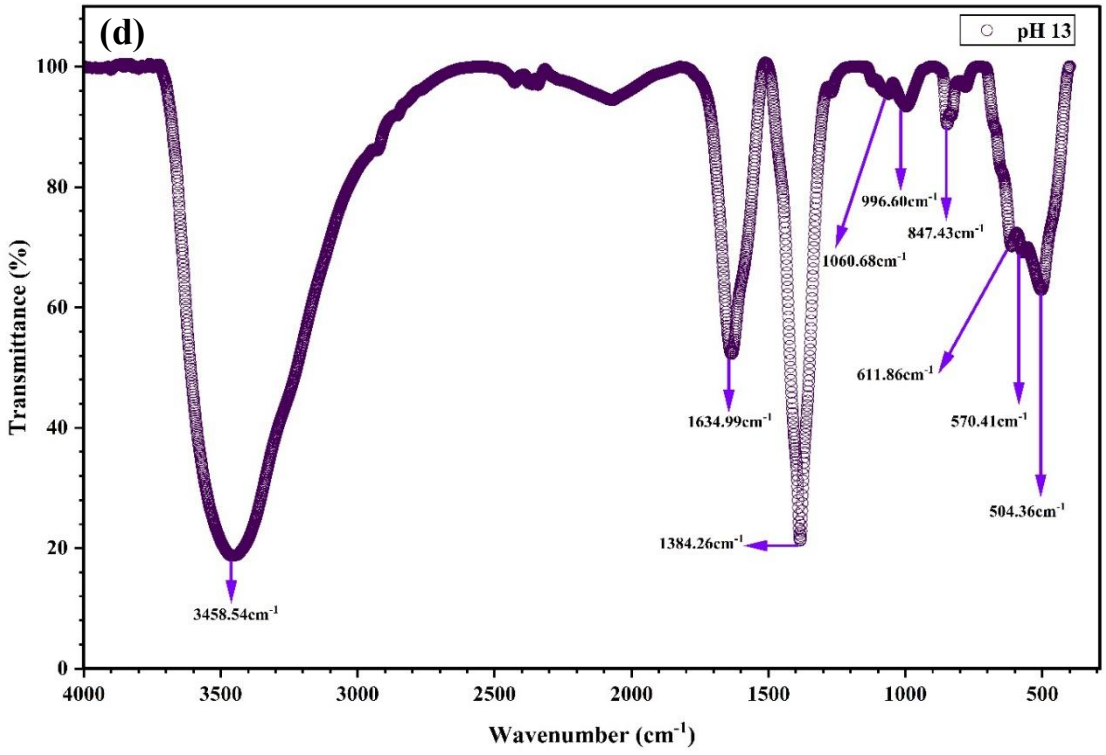
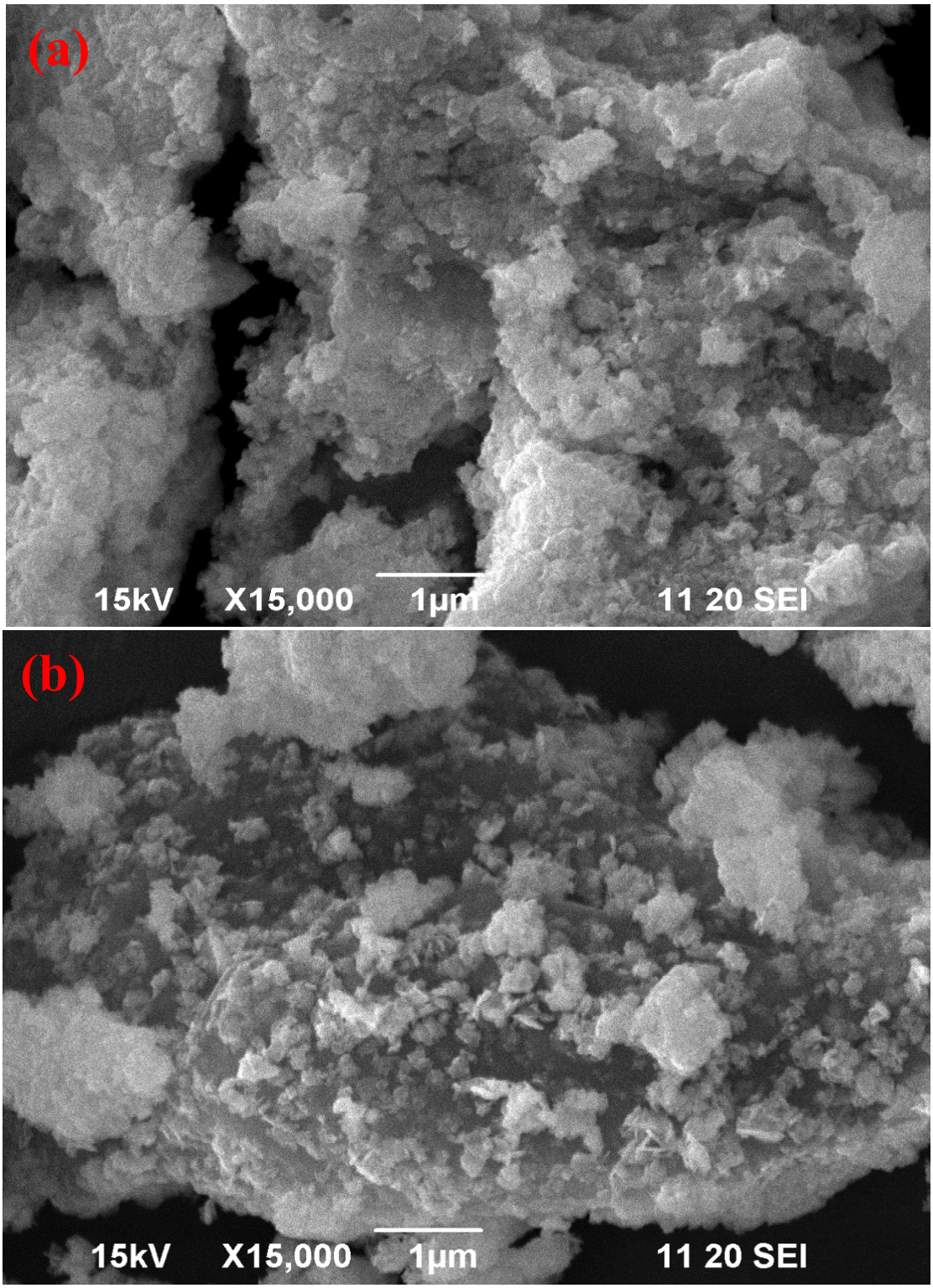
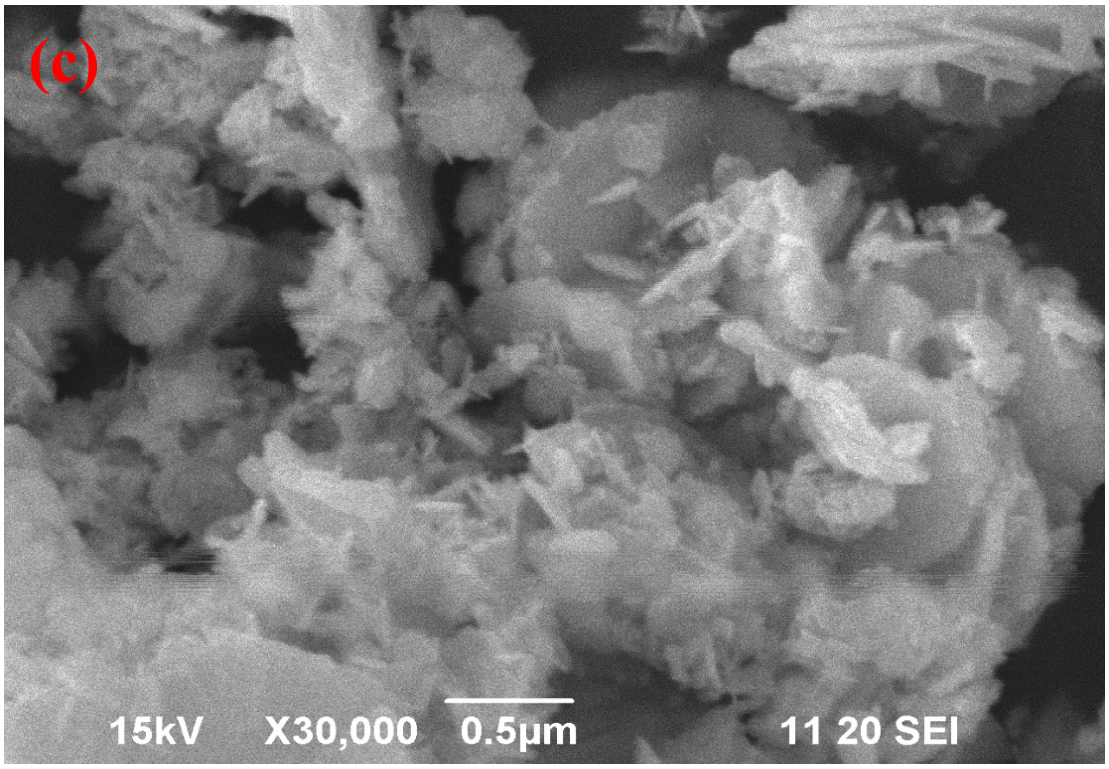
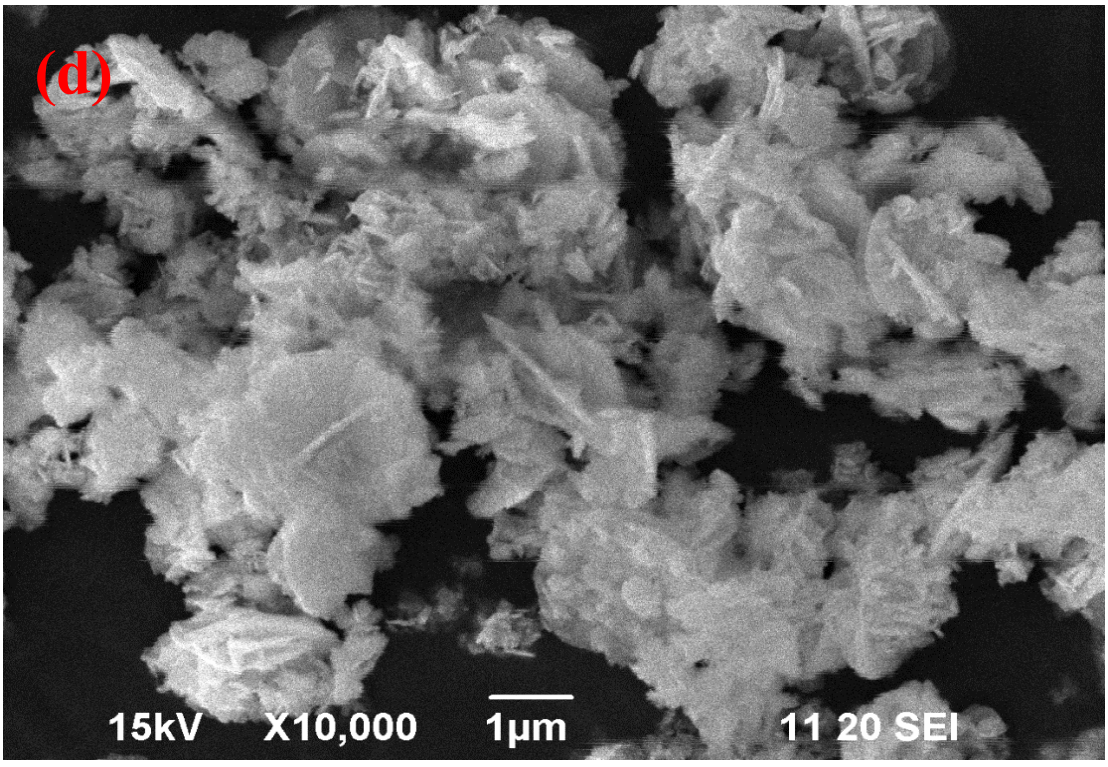
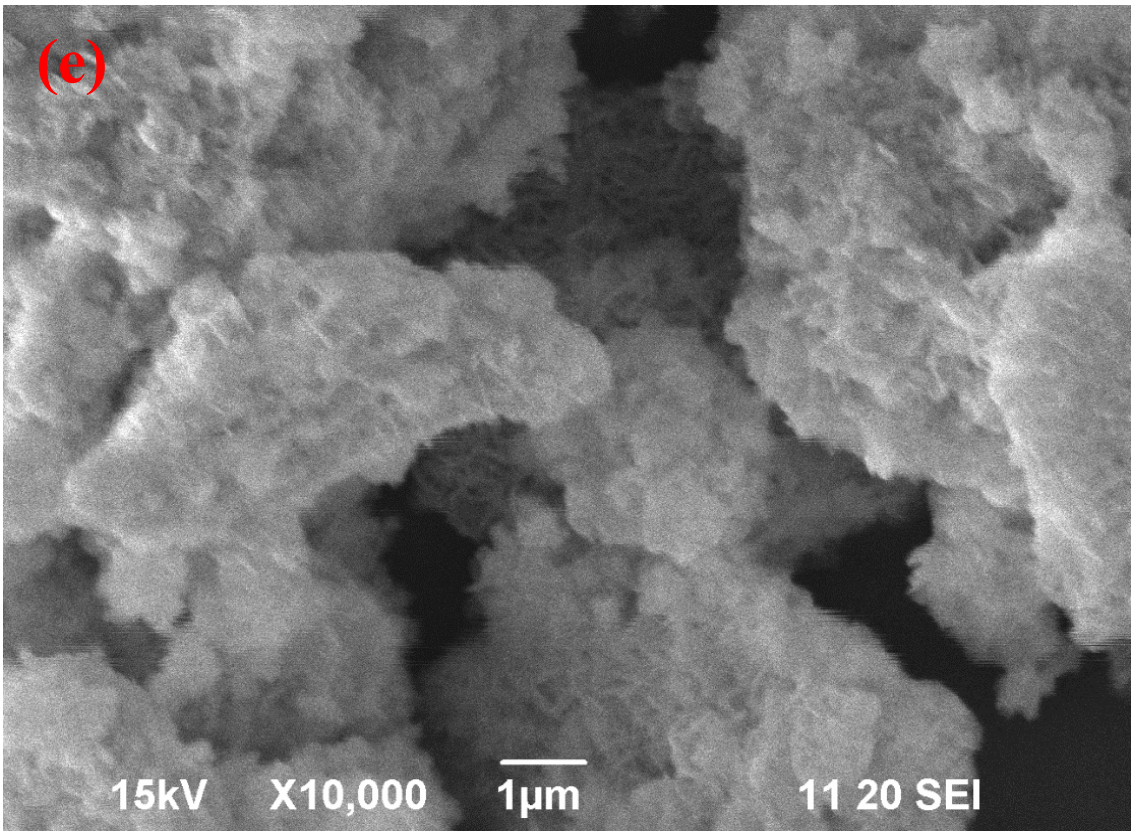

(d)
pH 13
Transmittance (%)
Wavenumber (cm-1)
3458.54cm-1
1634.99cm-1
1384.26cm-1
1060.68cm-1
996.60cm-1
847.43cm-1
611.86cm-1
570.41cm-1
504.36cm-1

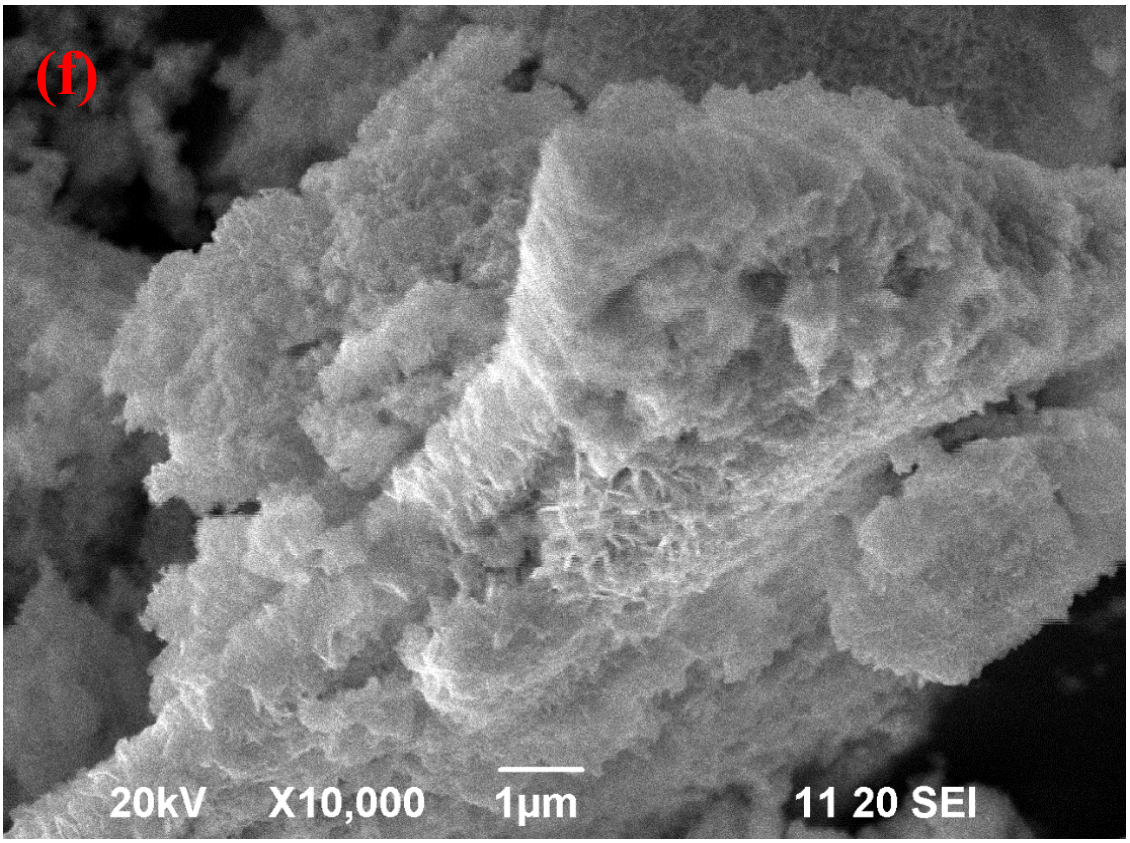
Figure 4. SEM micrographs of BiOI nanoparticles synthesized by maintaining pH conditions: (a-b) pH 5, (c-d) pH 8, (e-f) pH 10, and (g-h) pH 13.

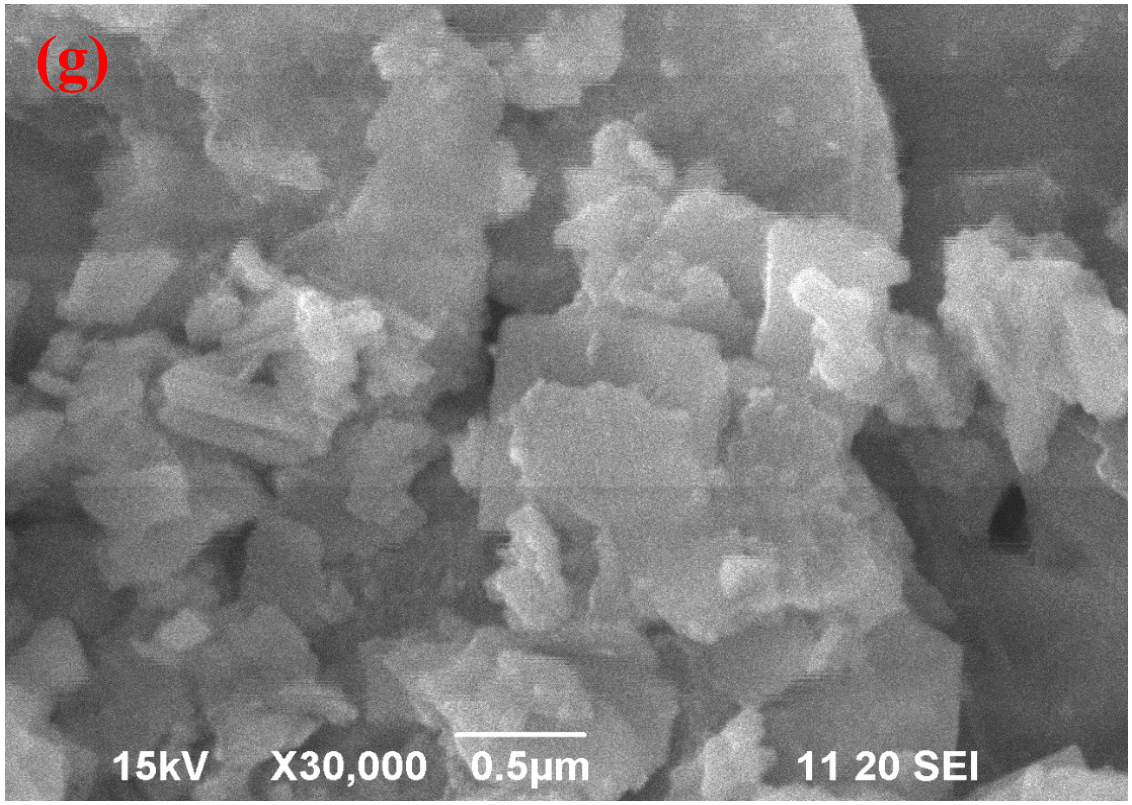



(c)
15kV X30,000 0.5µm 11 20 SEI


(d)
15kV X10,000 1µm 11 20 SEI


(e)
15kV X10,000 1μm 11 20 SEI


(f)
20kV X10,000 1μm 11 20 SEI


(g)
15kV X30,000 0.5µm 11 20 SEI

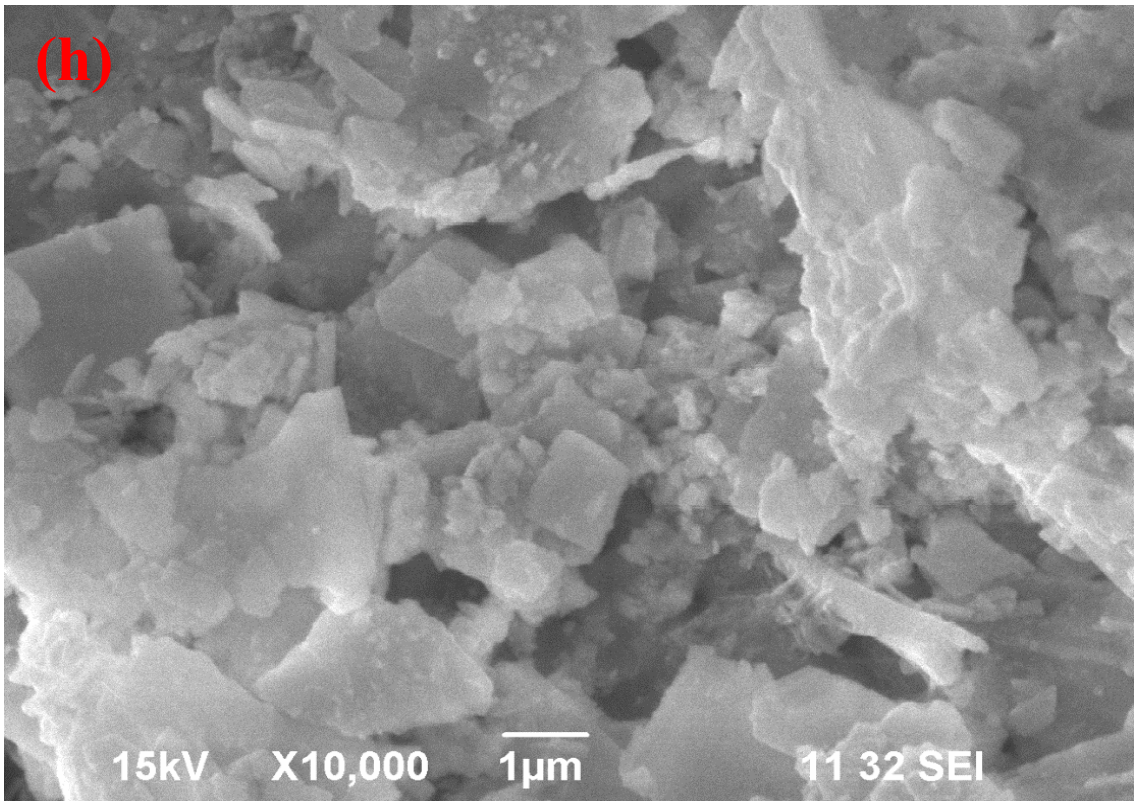
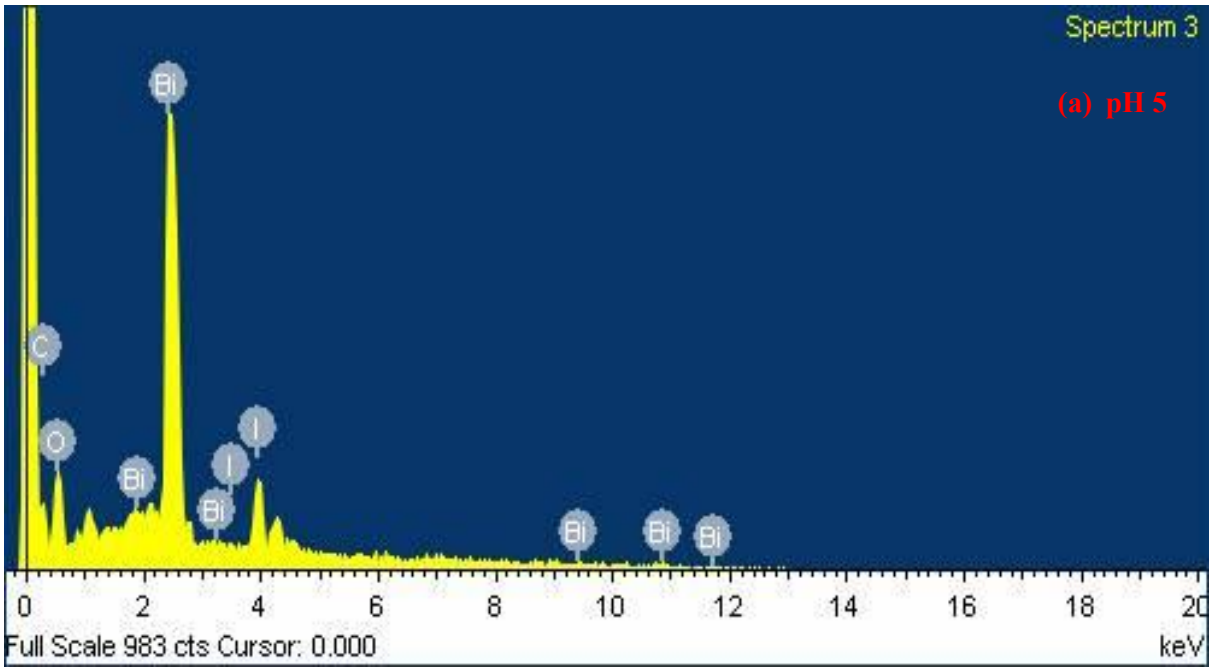
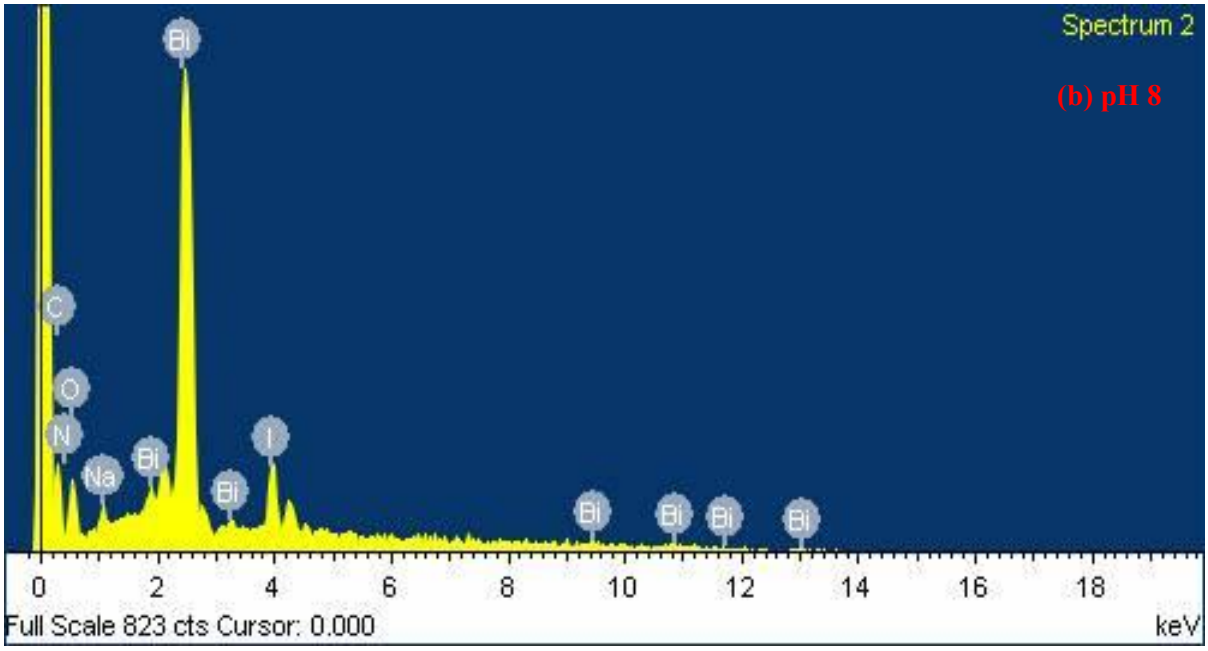
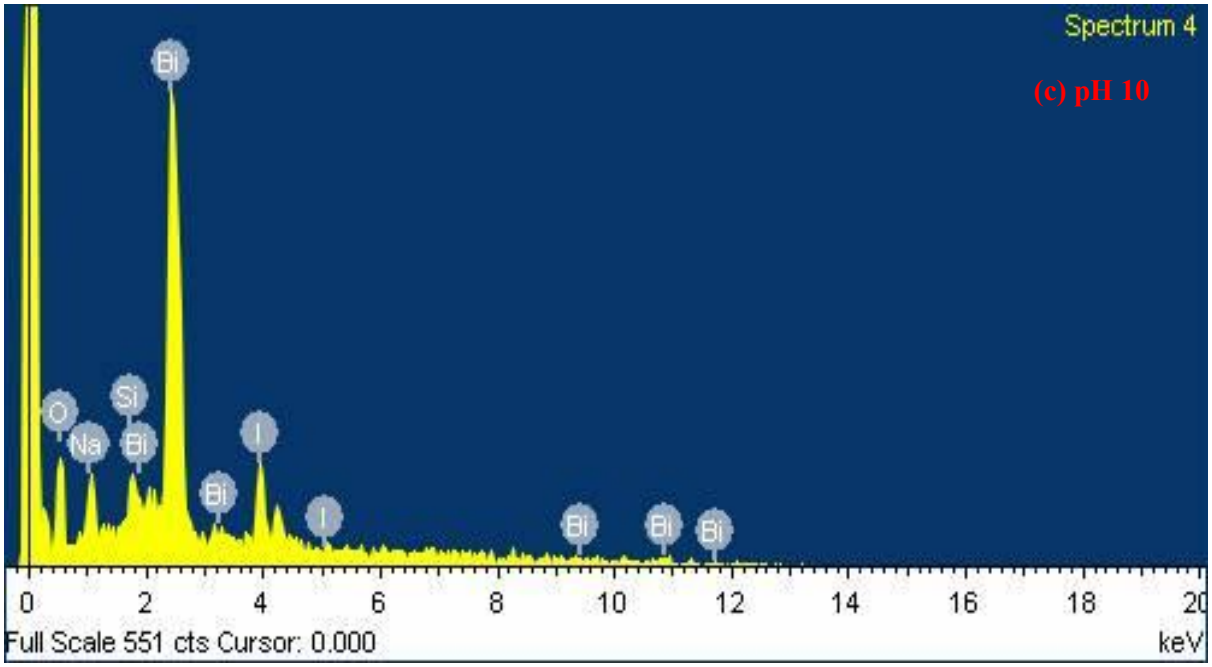

(h)
15kV X10,000 1µm 11 32 SEI

Figure 5. EDX spectra of BiOI nanoparticles synthesized at different pH conditions: (a) pH 5, (b) pH 8, (c) pH 10, and (d) pH 13.






Spectrum 4
(c) pH 10
Bi
O
Na
Si
Bi
Bi
I
I
Bi
Bi
Bi
0
2
4
6
8
10
12
14
16
18
Full Scale 551 cts Cursor: 0.000
keV

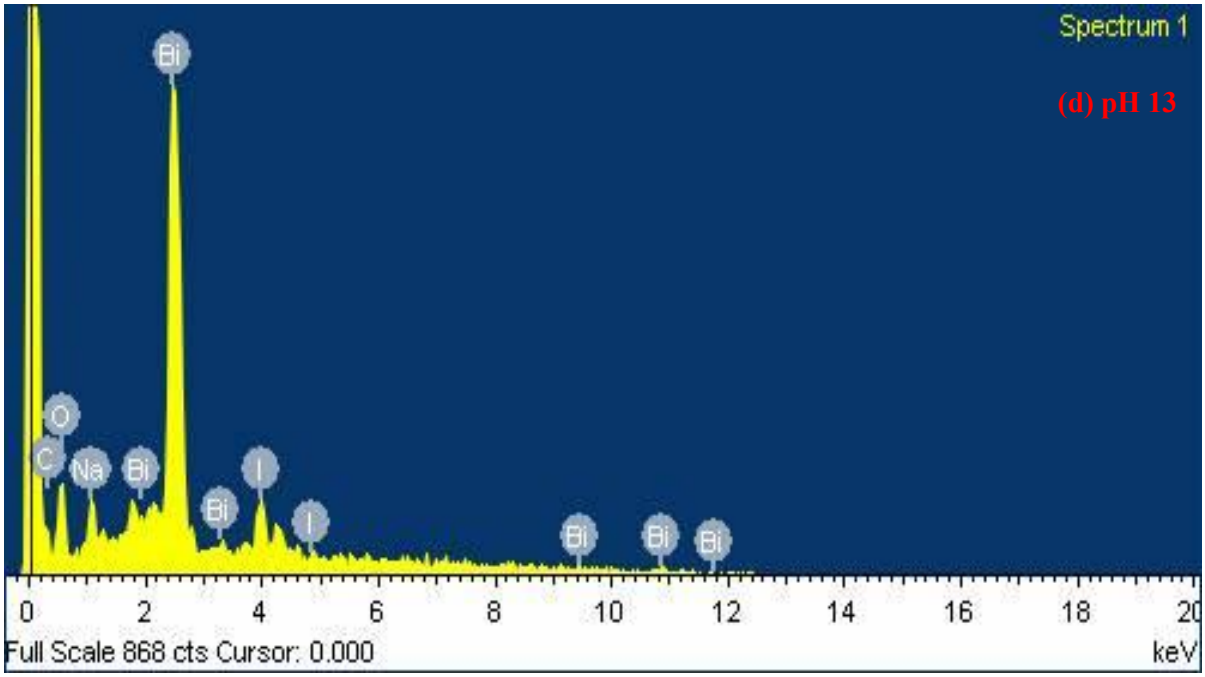
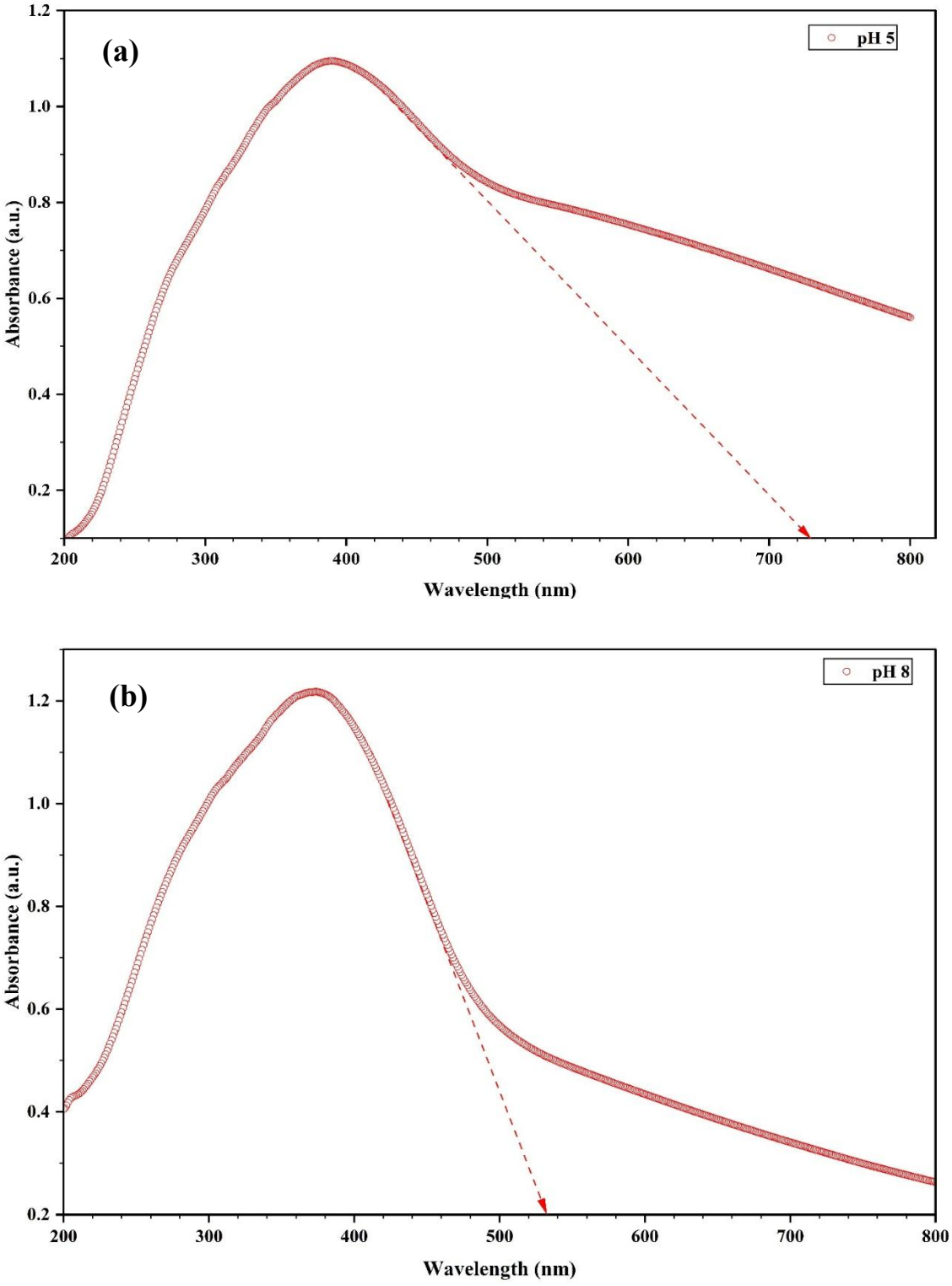
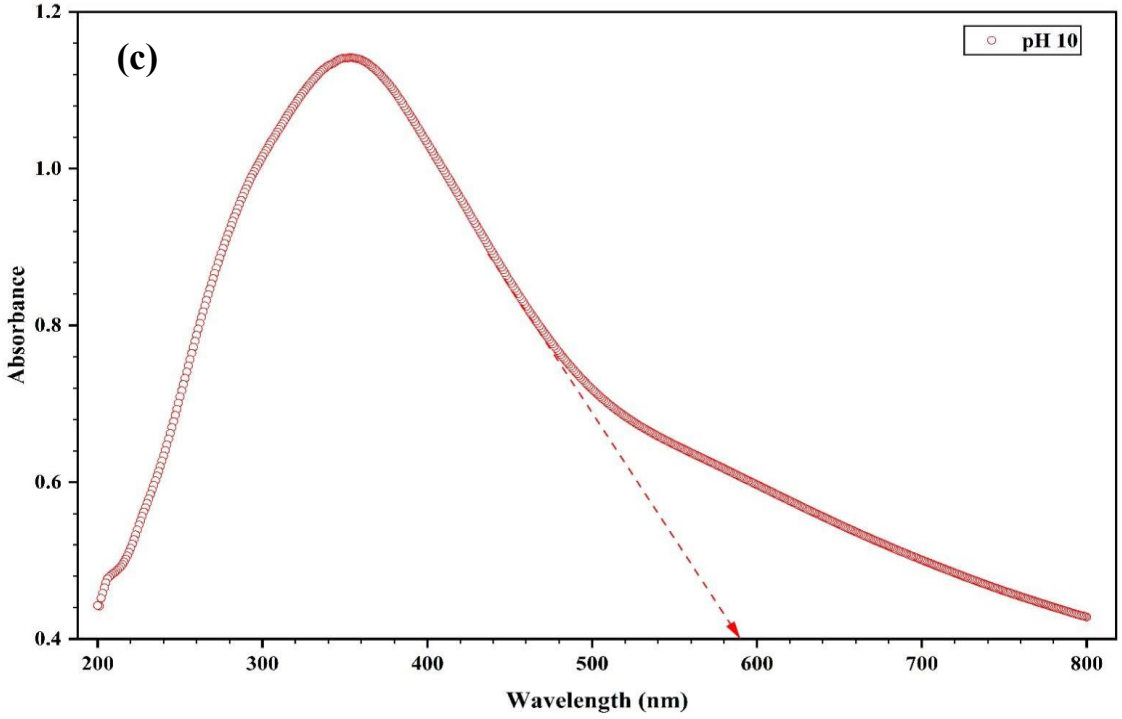

Spectrum 1
(d) pH 13
Bi
O
C
Na
Bi
Bi
I
I
Bi
Bi
Bi
0
2
4
6
8
10
12
14
16
18
Full Scale 868 cts Cursor: 0.000
keV

Figure 6. UV–Vis absorption spectra of BiOI nanoparticles synthesized at different pH conditions (a) pH 5, (b) pH 8, (c) pH 10, (d) pH 13; showing the variation in optical absorption behavior with wavelength.




(c)
pH 10
Absorbance
Wavelength (nm)
1.2
1.0
0.8
0.6
0.4
200
300
400
500
600
700
800

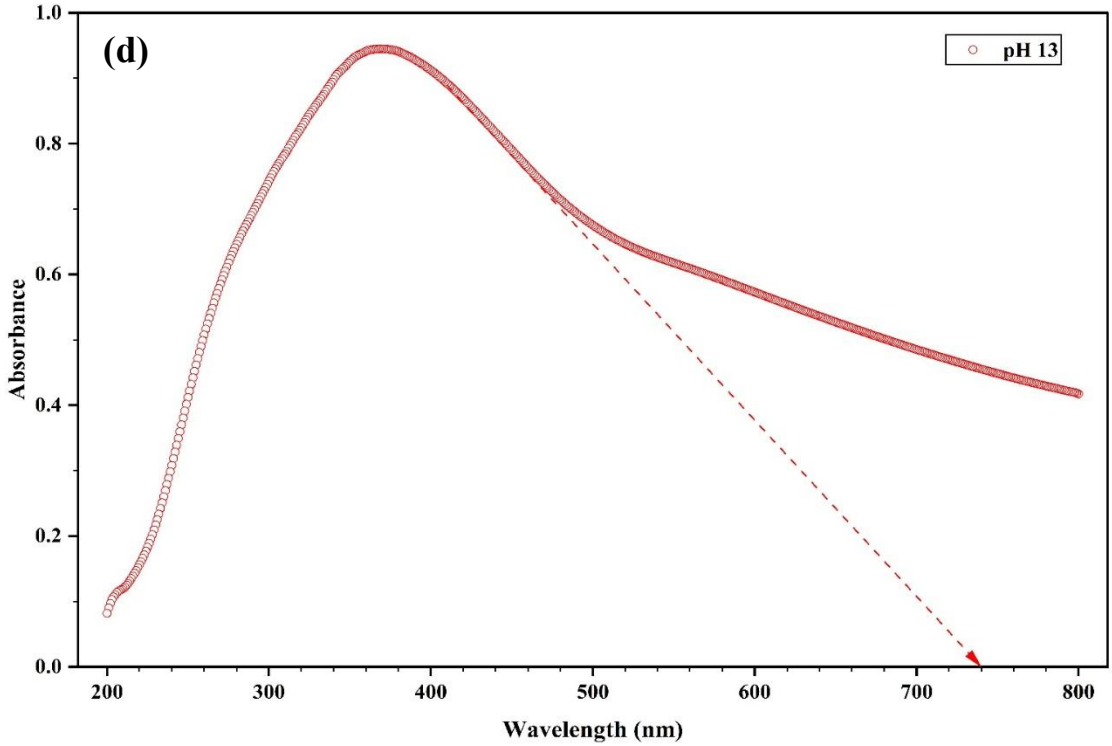
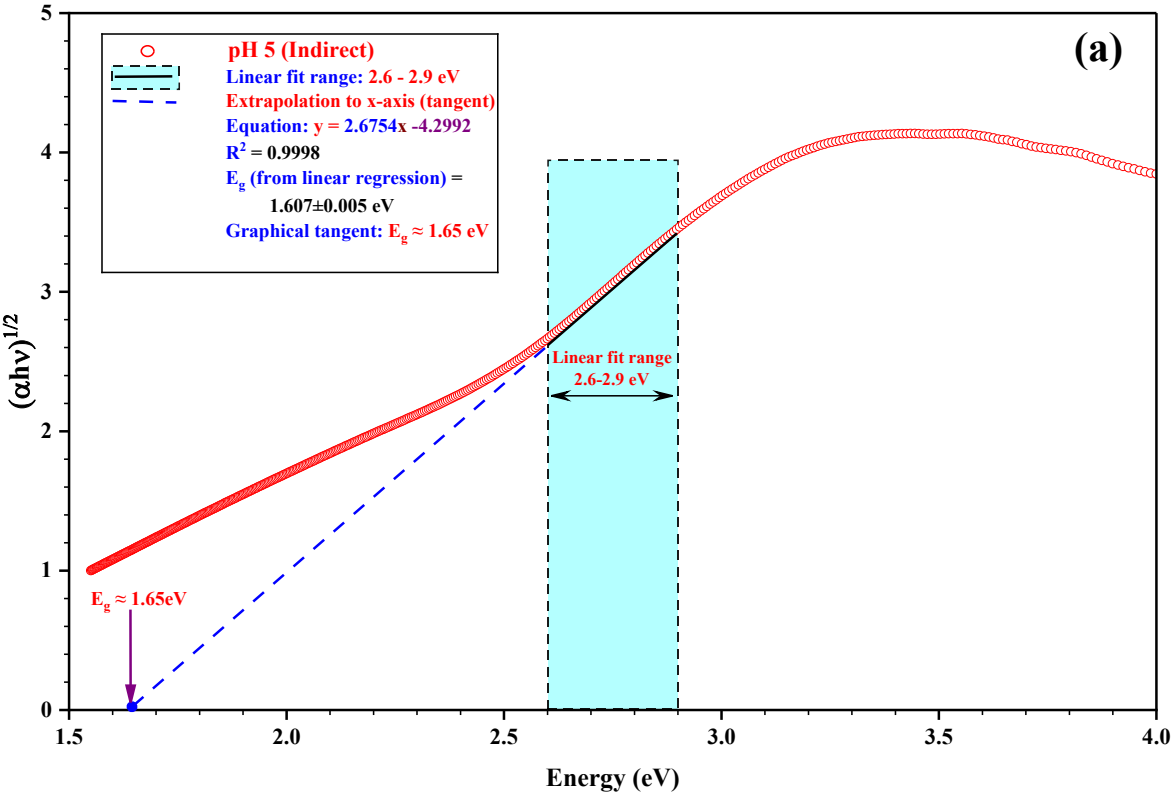
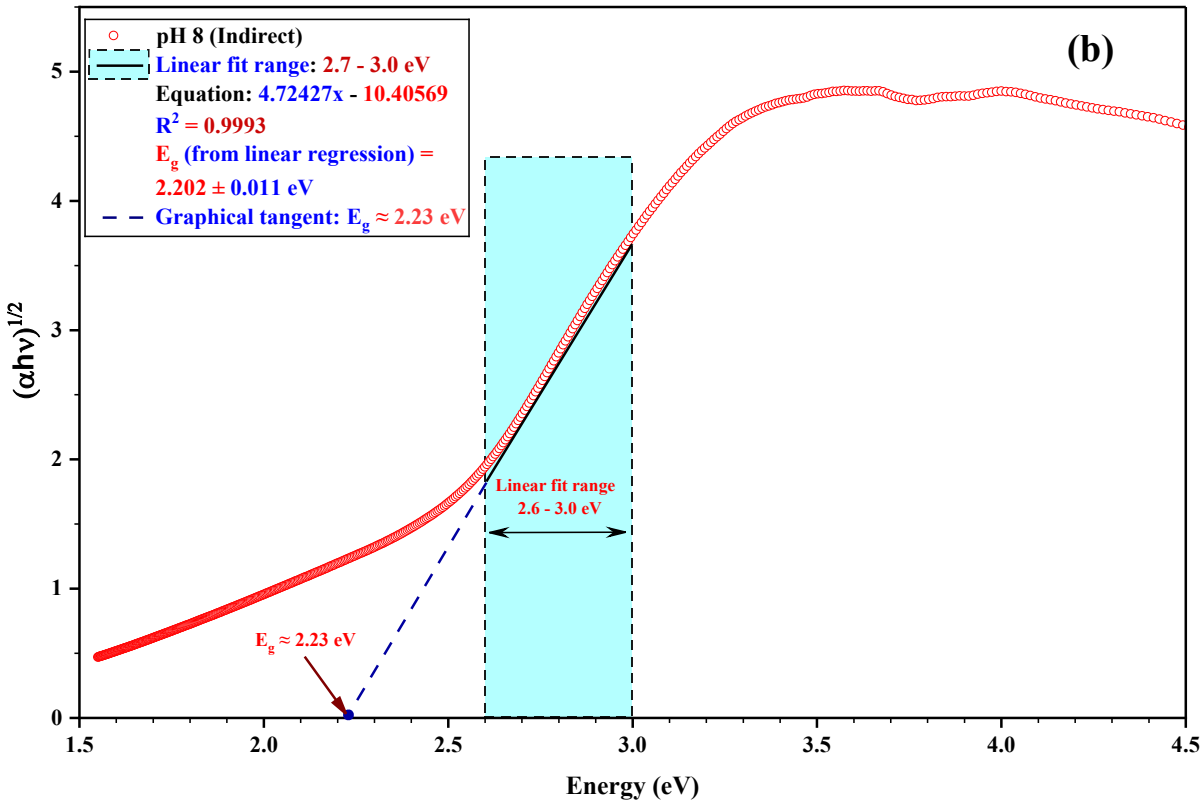
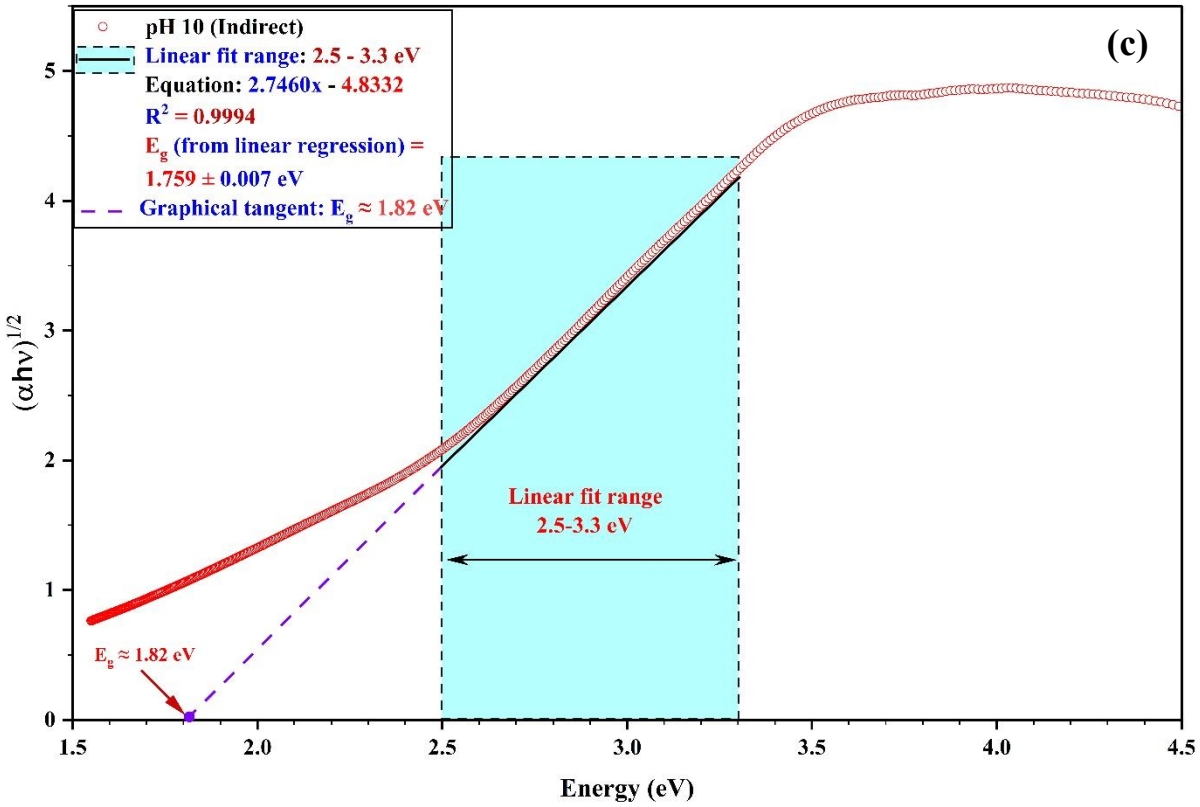

(d)
pH 13
Absorbance
Wavelength (nm)
1.0
0.8
0.6
0.4
0.2
0.0
200
300
400
500
600
700
800

Figure 7. Tauc plots of $(\alpha h\nu)^{1/2}$ versus photon energy (eV) for BiOI nanoparticles prepared at (a)pH 5, (b) pH 8, (c) pH 10, and (d) pH 13.




pH 8 (Indirect)
Linear fit range: 2.7 - 3.0 eV
Equation: 4.72427x - 10.40569
R2 = 0.9993
Eg (from linear regression) =
2.202 ± 0.011 eV
Graphical tangent: Eg ≈ 2.23 eV
(b)
Linear fit range
2.6 - 3.0 eV
Eg ≈ 2.23 eV
(αhν)1/2
Energy (eV)
0
1
2
3
4
5
1.5
2.0
2.5
3.0
3.5
4.0
4.5


pH 10 (Indirect)
Linear fit range: 2.5 - 3.3 eV
Equation: 2.7460x - 4.8332
R² = 0.9994
Eg (from linear regression) =
1.759 ± 0.007 eV
Graphical tangent: Eg ≈ 1.82 eV
(c)
Linear fit range
2.5-3.3 eV
Eg ≈ 1.82 eV
(αhν)^1/2
Energy (eV)
0
1
2
3
4
5
1.5
2.0
2.5
3.0
3.5
4.0
4.5

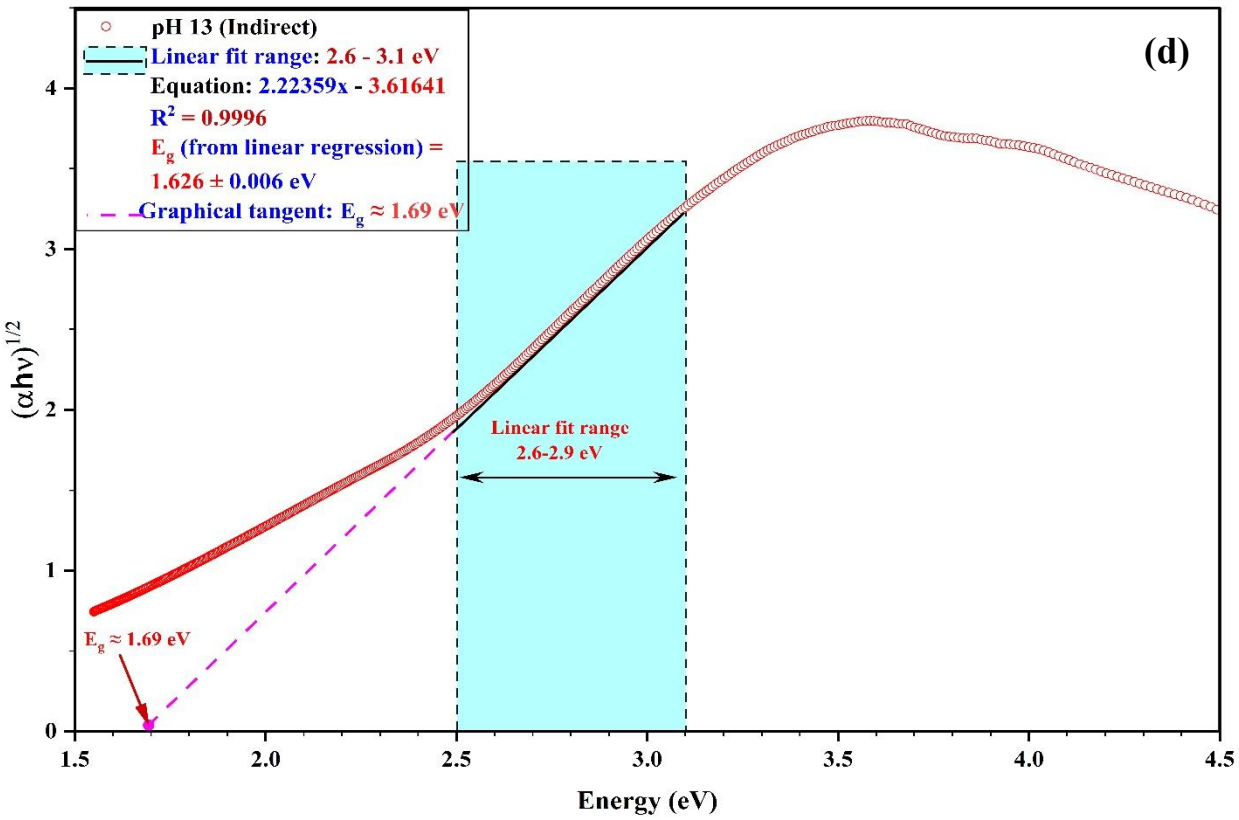
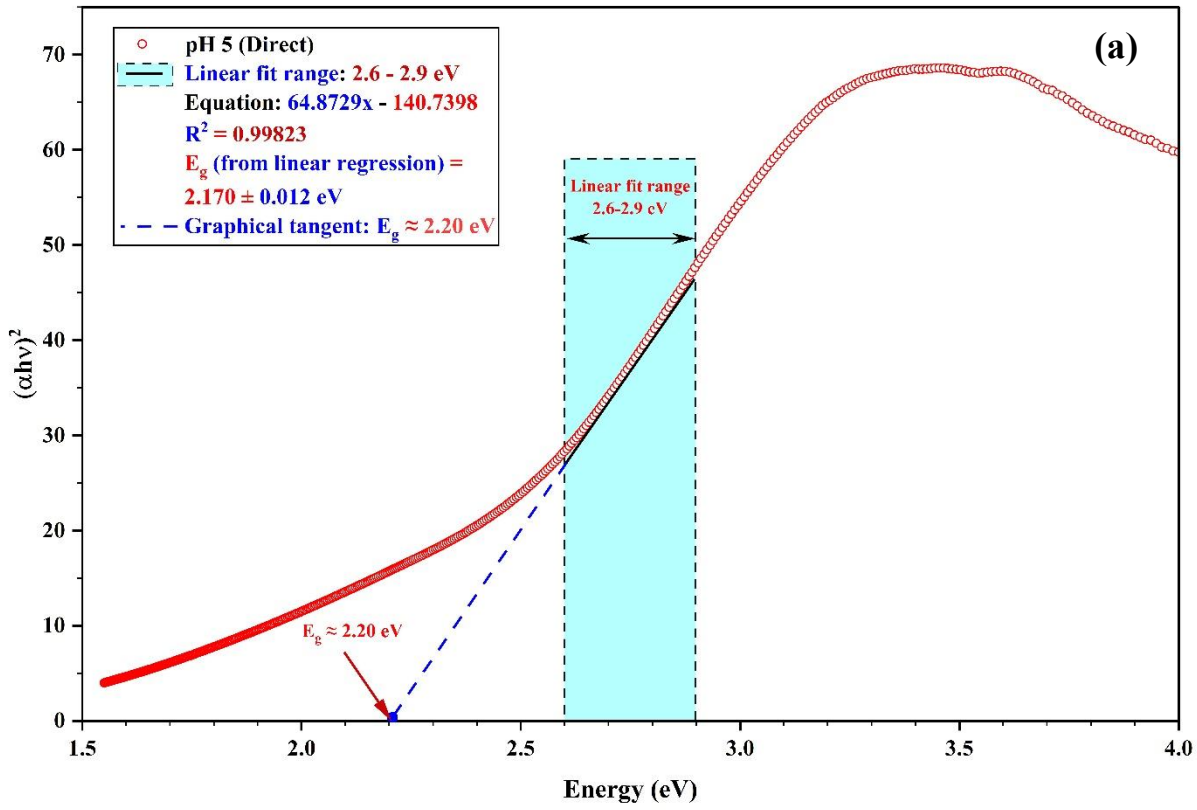
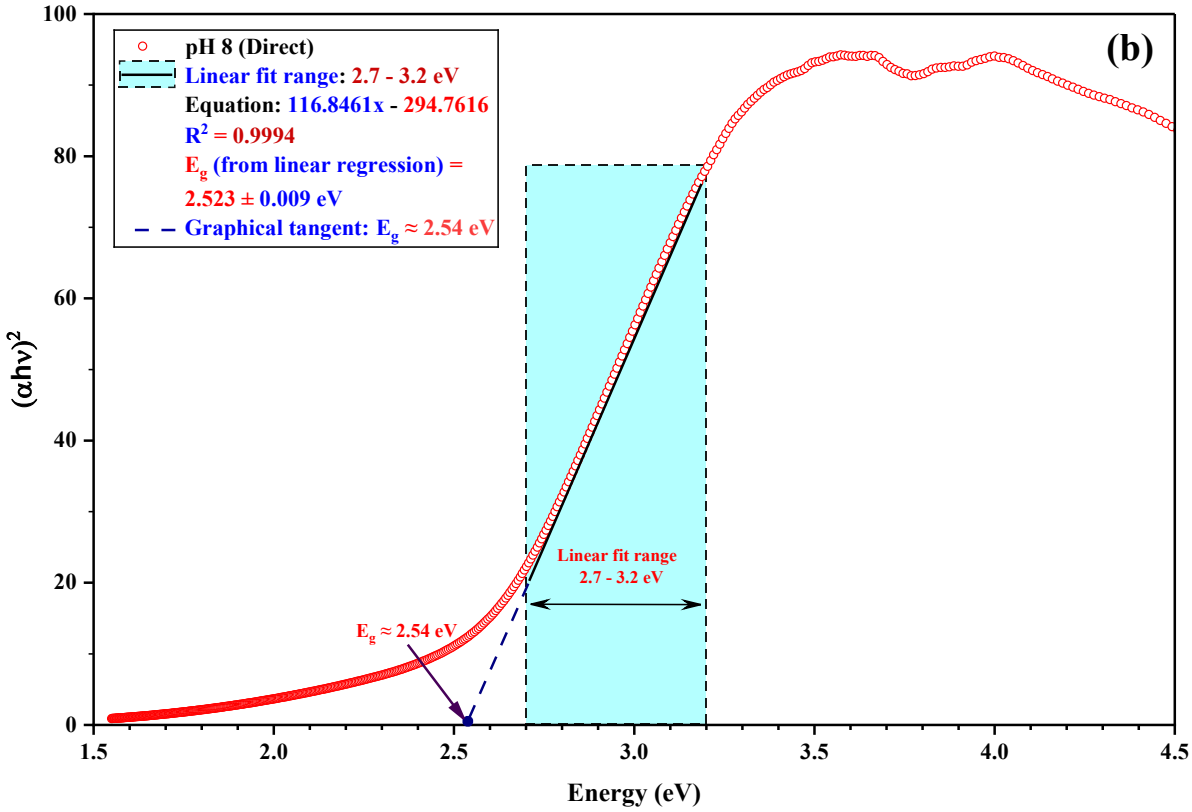
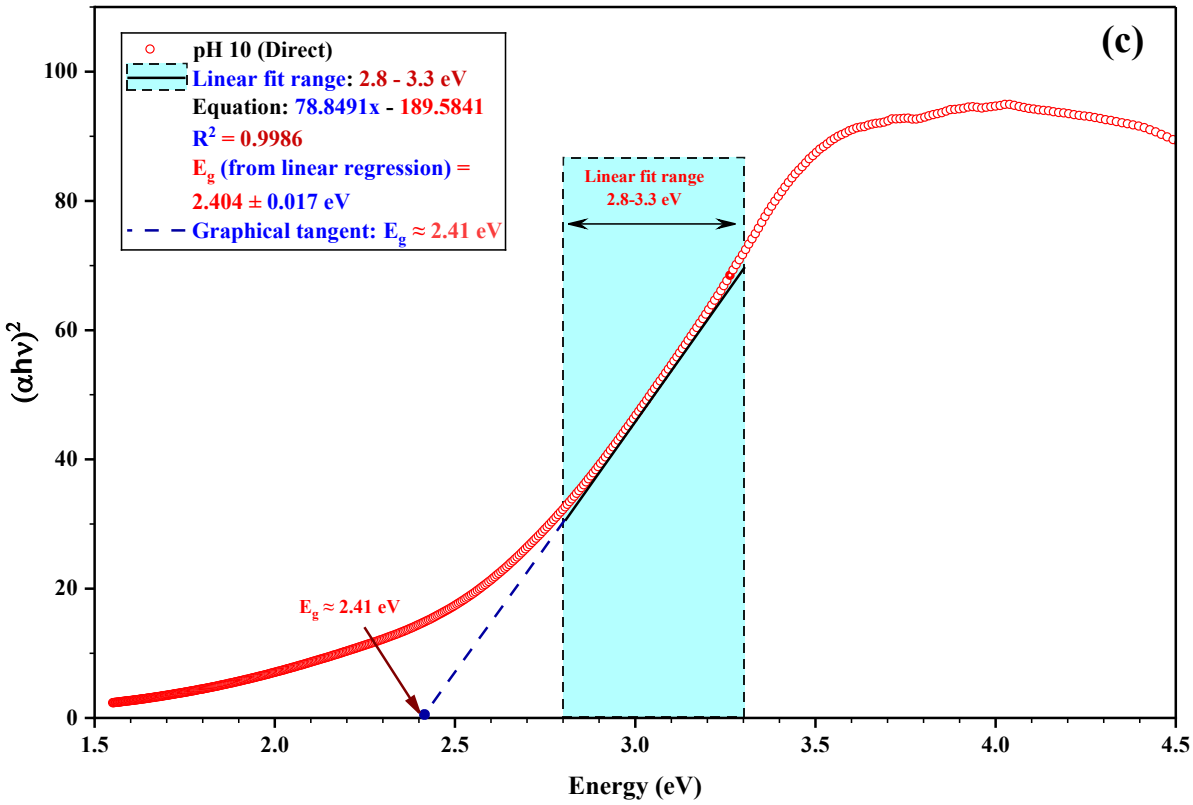

pH 13 (Indirect)
Linear fit range: 2.6 - 3.1 eV
Equation: 2.22359x - 3.61641
R² = 0.9996
Eg (from linear regression) =
1.626 ± 0.006 eV
Graphical tangent: Eg ≈ 1.69 eV
(d)
Linear fit range
2.6-2.9 eV
Eg ≈ 1.69 eV
(αhν)^1/2
Energy (eV)
0
1
2
3
4
1.5
2.0
2.5
3.0
3.5
4.0
4.5

Figure.8. Tauc plots of $(\alpha h\nu)^2$ versus photon energy (E) for BiOI nanoparticles prepared at (a)pH 5, (b) pH 8, (c) pH 10, and (d) pH 13.




(b)
pH 8 (Direct)
Linear fit range: 2.7 - 3.2 eV
Equation: 116.8461x - 294.7616
R² = 0.9994
Eg (from linear regression) =
2.523 ± 0.009 eV
Graphical tangent: Eg ≈ 2.54 eV
Linear fit range
2.7 - 3.2 eV
Eg ≈ 2.54 eV
(αhν)²
Energy (eV)
0
20
40
60
80
100
1.5
2.0
2.5
3.0
3.5
4.0
4.5


(c)
pH 10 (Direct)
Linear fit range: 2.8 - 3.3 eV
Equation: 78.8491x - 189.5841
R² = 0.9986
Eg (from linear regression) =
2.404 ± 0.017 eV
Graphical tangent: Eg ≈ 2.41 eV
Linear fit range
2.8-3.3 eV
Eg ≈ 2.41 eV
(αhν)²
Energy (eV)
0
20
40
60
80
100
1.5
2.0
2.5
3.0
3.5
4.0
4.5

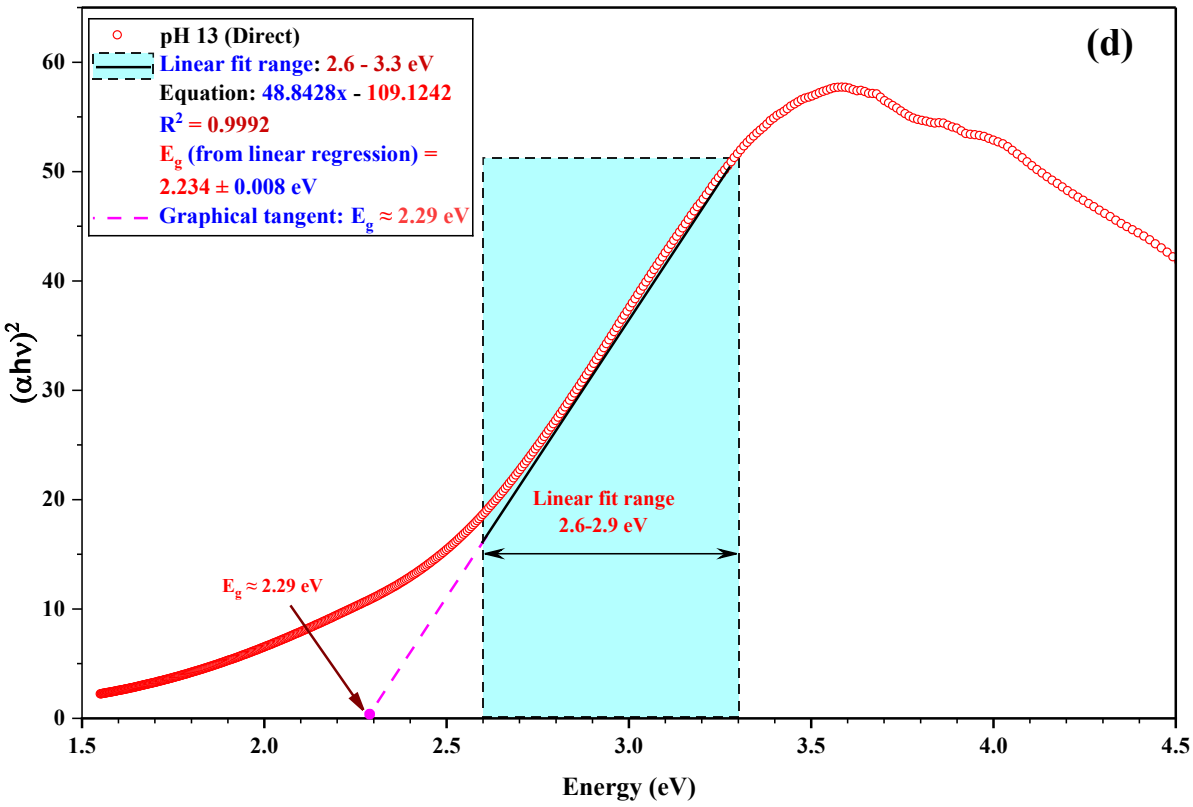
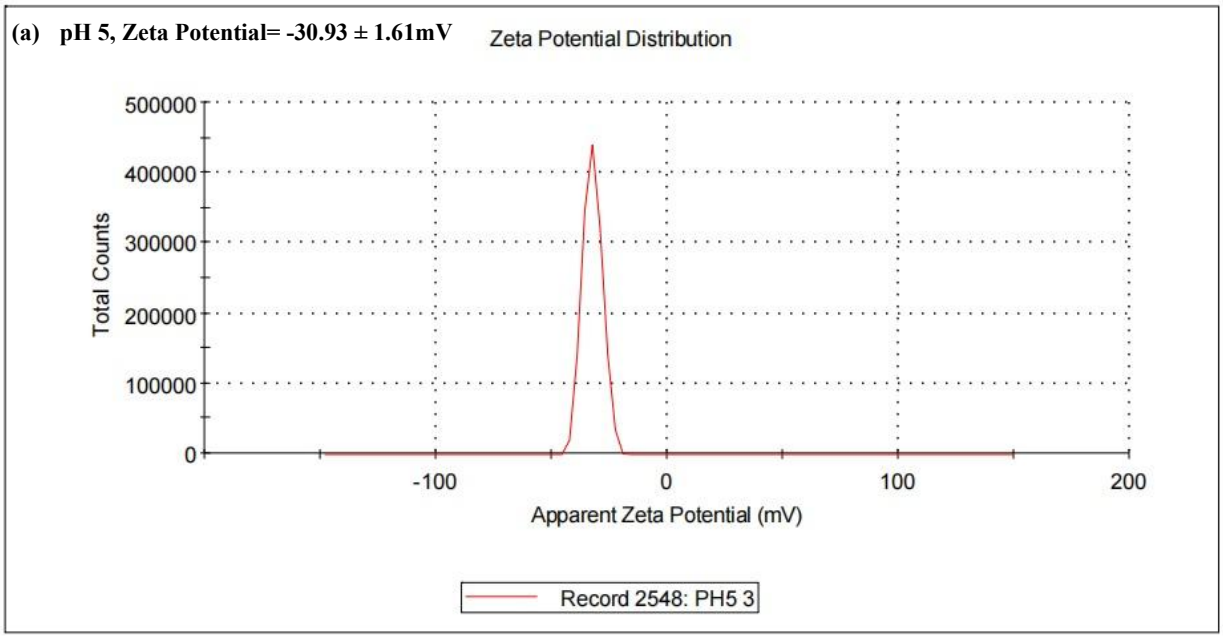
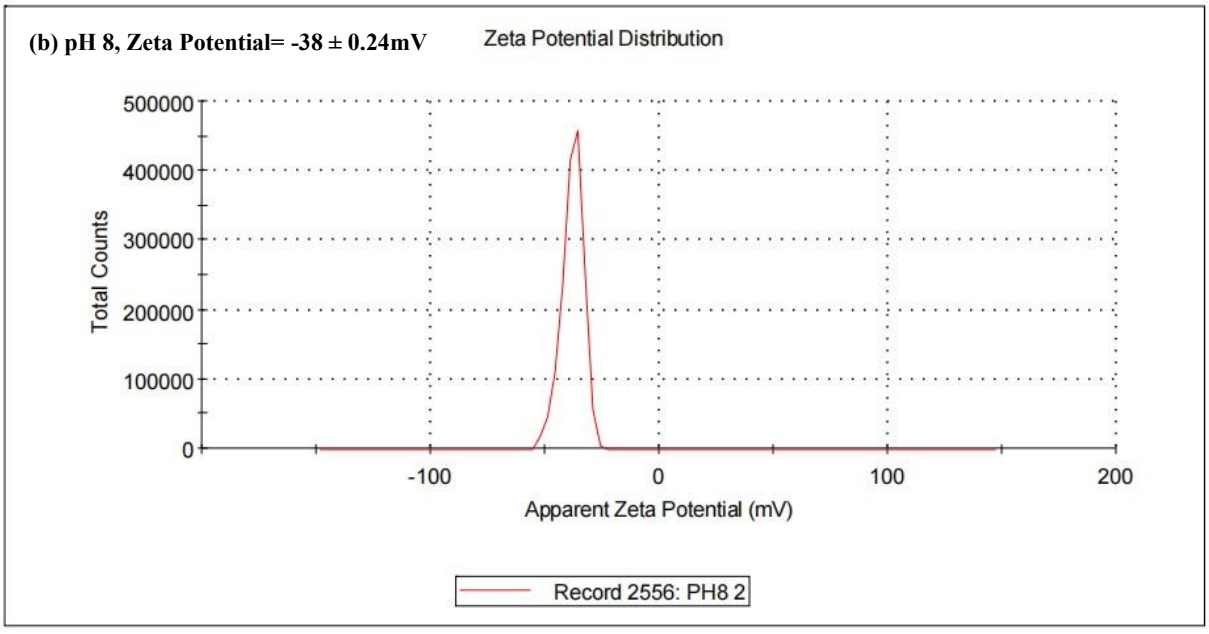
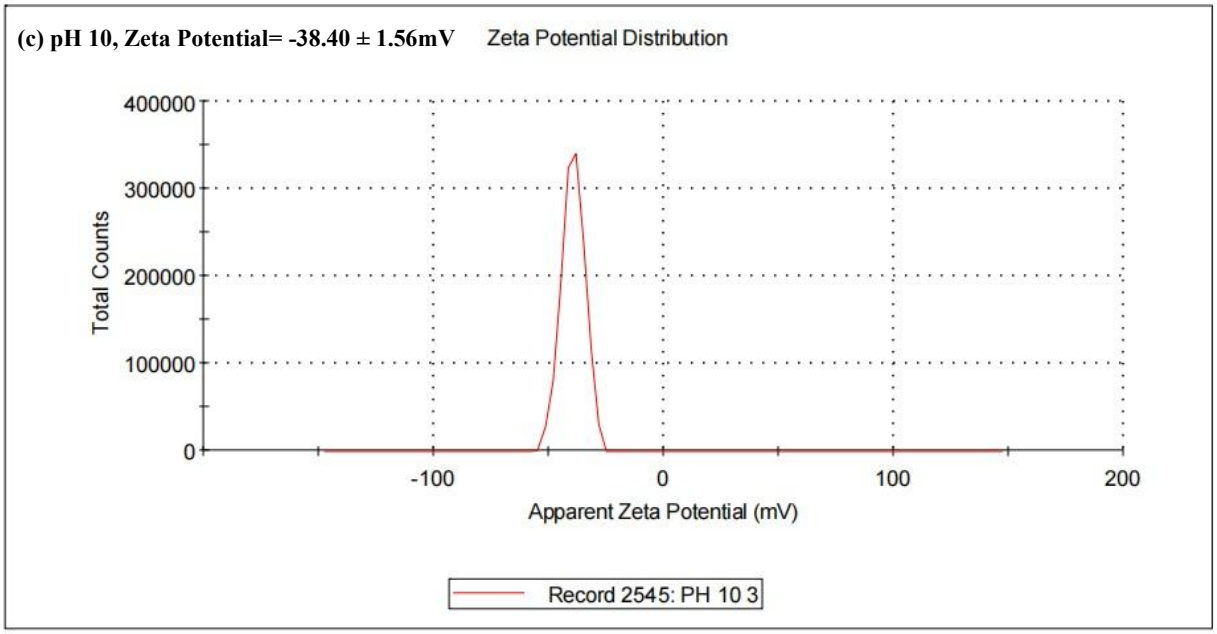

(d)
pH 13 (Direct)
Linear fit range: 2.6 - 3.3 eV
Equation: 48.8428x - 109.1242
R² = 0.9992
Eg (from linear regression) =
2.234 ± 0.008 eV
Graphical tangent: Eg ≈ 2.29 eV
Linear fit range
2.6-2.9 eV
Eg ≈ 2.29 eV
(αhν)²
Energy (eV)
0
10
20
30
40
50
60
1.5
2.0
2.5
3.0
3.5
4.0
4.5

Figure 9. Zeta potential analysis of BiOI nanoparticles synthesized at different pH conditions: (a) pH 5, (b) pH 8, (c) pH 10, and (d) pH 13





(c) pH 10, Zeta Potential= -38.40 ± 1.56mV



(d) pH 13, Zeta Potential= -40.83 ± 0.34mV

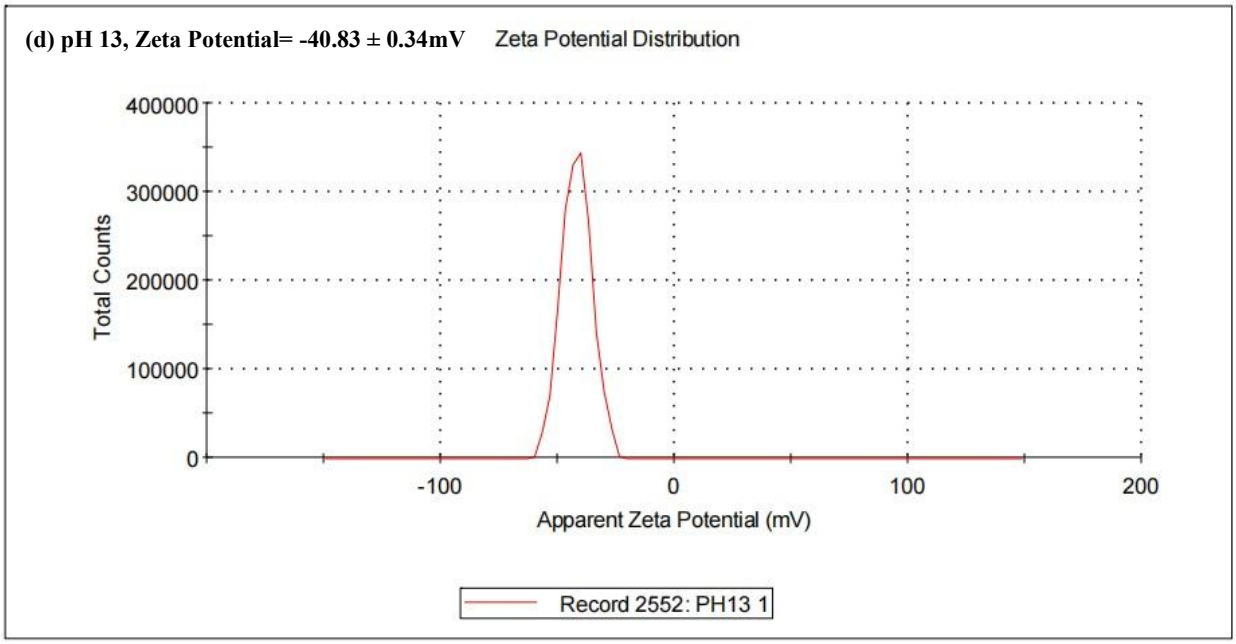
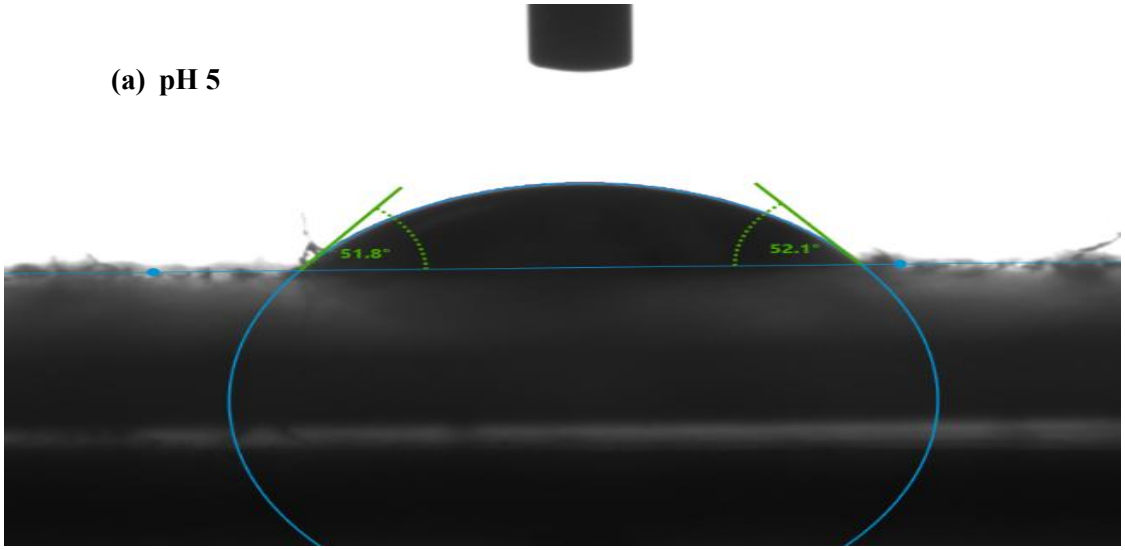
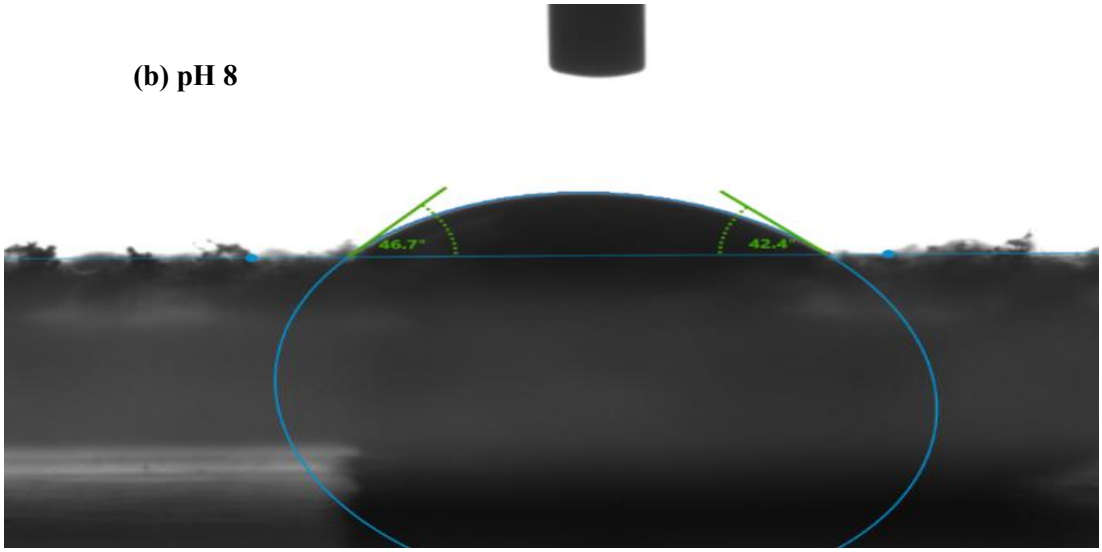


Figure 10. Contact angle measurements of BiOI nanoparticles (deposited on glass substrate) synthesized at different pH conditions: (a) pH 5, (b) pH 8, (c) pH 10, and (d) pH 13.

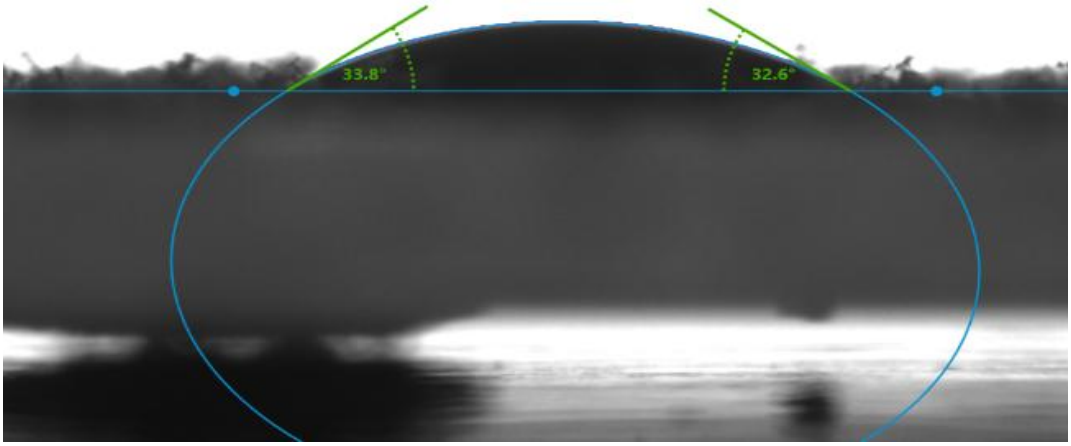
(a) pH 5



(b) pH 8



(c) pH 10



(d) pH 13

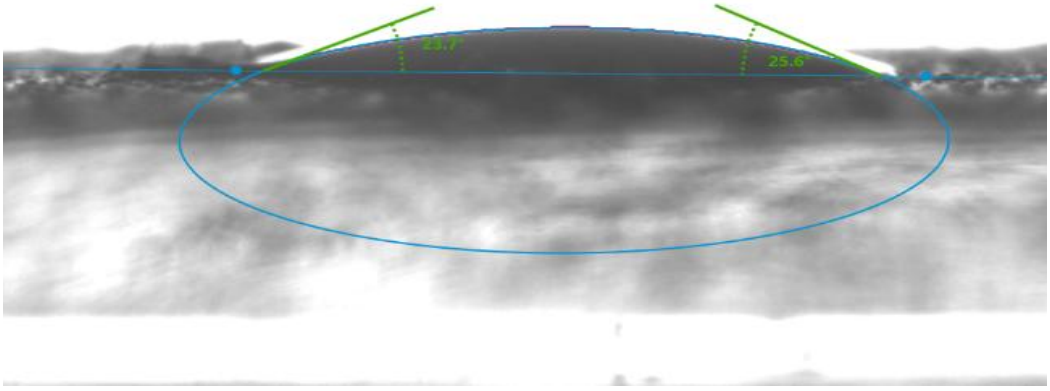


Table 1. XRD peak positions (2θ), interplanar spacing (d), and corresponding crystallographic (hkl) planes of BiOI nanomaterials synthesized at different pH levels.

Crystal Structure	**Pure Tetragonal**									**Orthorhombic**		
pH	**5**			**8**			**10**			**13**		
JCPDS Card No.												
10-0445, 40-0548, and 73-2062	2θ	d-spacing (Å)	hkl	2θ	d-spacing (Å)	hkl	2θ	d-spacing (Å)	hkl	2θ	d-spacing (Å)	hkl
	23.80	6.89	101	23.88	3.72	101	12.46	7.09	001	10.98	8.04	200
	29.19	3.73	102	29.01	3.07	102	23.85	3.72	101	28.18	3.16	312
	31.75	2.81	110	31.71	2.81	110	29.76	2.99	102	31.18	2.86	004
	39.02	2.30	004	37.19	2.41	103	32.71	2.73	110	33.13	2.69	204
	45.42	1.99	200	42.18	2.14	104	41.72	2.16	112	33.54	2.66	020
	54.80	1.67	212	45.43	1.99	200	46.90	1.93	200	46.27	1.96	223
				49.63	1.84	055/211	56.54	1.62	212	47.83	1.90	315
				54.76	1.67	212				53.56	1.70	622
										58.71	1.58	516

Table 2. Structural and nanocrystalline parameters of BiOI nanomaterials at different pH values, including crystallite size (D), dislocation density (δ), microstrain (ε), percentage crystallinity, and lattice parameters (a and c), highlighting the influence of pH on crystallinity, defect density, and structural tuning.

Composition	**pH**	**D nm**	**δ (10^{15}) m^{-2}**	**ϵ (10^{-3})**	**% Crystallinity**	**Lattice parameter (Å)**		
						a	**b**	**c**
BiOI/Bi_5O_7I	5	25.30±7.82	2.09	5.27	97.75	3.98	3.98	9.23
	8	18.67±4.86	3.46	6.14	92.42	3.99	3.99	9.45
	10	20.37±4.86	2.96	7.12	86.92	3.87	3.87	8.75
	13	30.37±11.34	1.80	4.39	95.37	16.09	5.34	11.46

Table 3. Assignment of the characteristic FTIR absorption bands of green-synthesized BiOI nanoparticles prepared at different reaction pH values (5, 8, 10, and 13), along with their corresponding vibrational modes and chemical bond assignments.

Assignment	pH 5 (cm^{-1})	pH 8 (cm^{-1})	pH 10 (cm^{-1})	pH 13 (cm^{-1})	Reference(s)
O–H stretching vibration (surface hydroxyl groups and phytochemicals)	3423.49	3247.89	3432.43	3458.54	[35-36]
H–O–H bending vibration (adsorbed water)	1628.47	1633.34	1631.76	1634.99	[32], [35]
NO_3^- asymmetric stretching vibration	1383.95	1382.88	1382.83	1384.26	[29], [32], [35]
Bi–O stretching vibration ($[Bi_2O_2]$ layer / Bi–O coordination)	1012.09	1058.01	1015.89	1060.68	[32-33], [36-38]
Bi–O stretching vibration	—	—	—	996.60	[38]
Additional Bi–O–I lattice vibration	—	—	897.39	—	[35,38]
Bi–O–I lattice vibration	838.80	846.86	844.37	847.43	[32-33], [36,38]
Bi–O lattice vibration	666.54	—	455.52	611.86, 570.41	[35-38]
Bi–I lattice vibration	536.72	548.89	536.47	504.36	[35,38]

Table 4. Apparent optical transition energies obtained from linear regression and graphical tangent extrapolation, together with the coefficients of determination (R^2) and linear fitting ranges for BiOI nanoparticles synthesized at different pH values.

pH	Bandgap (Regression) eV		Bandgap (Tangent) eV		Coefficient of Determination (R^2)		Fitting Range	
	Indirect	Direct	Indirect	Direct	Indirect	Direct	Indirect	Direct
5	1.607 ± 0.005	2.170 ± 0.012	1.65	2.20	0.99989	0.99823	2.6-2.9	2.6-2.9
8	2.202 ± 0.011	2.523 ± 0.009	2.23	2.54	0.99928	0.99942	2.7-3.0	2.7-3.2
10	1.759 ± 0.007	2.404 ± 0.017	1.82	2.41	0.99941	0.99866	2.5-3.3	2.8-3.3
13	1.626 ± 0.006	2.234 ± 0.008	1.69	2.29	0.99964	0.99922	2.5-3.1	2.6-3.3

Table 5. Zeta potential values of BiOI/Bi_5O_7I samples synthesized at different pH conditions. The measurements were performed in triplicate, and the results are presented as mean ± standard deviation (n = 3).

Sample	**Zeta potential (mV)**			**Zeta Potential** (Mean ± SD) mV
	Run 1	**Run 2**	**Run 3**	
BiOI pH-5	-29.1	-31.6	-32.1	-30.93 ± 1.61
BiOI pH-8	-38.6	-37.8	-37.7	-38.03 ± 0.24
BiOI pH-10	-36.6	-39.2	-39.4	-38.40 ± 1.56
Bi_5O_7I pH-13	-41.7	-40.5	-40.3	-40.83 ± 0.34

Table 6. Water contact-angle values of BiOI/Bi_5O_7I samples synthesized at different pH conditions. Measurements were performed at two different locations on each sample surface, with left and right contact angles measured for each droplet. The average of the left and right angles was used for each location, and the final values are presented as mean ± standard deviation (n = 2).

Sample	**Average Contact Angle (°)**		**Contact angle (Mean ± SD)°**
	Measurement 1	**Measurement 2**	
BiOI pH-5	51.95	55.20	53.57 ± 2.23
BiOI pH-8	42.40	44.55	43.47 ± 1.52
BiOI pH-10	33.20	29.95	31.57 ± 2.29
Bi_5O_7I pH-13	24.65	21.40	23.03 ± 2.29